THE ASTROPHYSICAL JOURNAL, 371:541–562, 1991 April 20

ULTRAVIOLET VARIABILITY OF NGC 5548: DYNAMICS OF THE CONTINUUM PRODUCTION REGION AND GEOMETRY OF THE BROAD-LINE REGION

J. H. KROLIK
Department of Physics and Astronomy, Johns Hopkins University, Baltimore, MD 21218
KEITH HORNE
Space Telescope Science Institute, 3700 San Martin Drive, Baltimore, MD 21218
T. R. KALLMAN
NASA Goddard Space Flight Center, Code 665, Greenbelt, MD 20771
M. A. MALKAN
Department of Astronomy, University of California, Los Angeles, CA 90024
R. A. EDELSON
Center for Astrophysics and Space Astronomy, University of Colorado, Boulder, CO 80309
AND
G. A. KRISS
Department of Physics and Astronomy, Johns Hopkins University, Baltimore, MD 21218
Received 1990 May 2; accepted 1990 September 28

ABSTRACT

We have used the data obtained in the 1989–1990 *IUE* monitoring of NGC 5548 to derive a mean shape for the ionizing spectrum; mean line profiles; the continuum fluctuation power spectrum in three UV bands; cross-correlation functions relating these bands; cross-correlation functions relating fluctuations in eight emission lines to fluctuations in the UV continuum; and the response functions through which the continuum fluctuations appear to generate the fluctuations in each of these eight lines.

The mean shape of the UV continuum is well fit by an accretion disk model with a black hole mass of $1 \times 10^8 h^{-1}/\sin i\ M_\odot$; however, an additional component is required to reproduce the observed soft X-ray flux. Construction of mean line profiles gives both a separation of the broad and narrow components in the lines and also a measurement of the velocity widths for the broad components. The widths of the lines increase with increasing ionization stage.

We find that the continuum fluctuation power spectrum is very steep, with most of the variance coming from ~ 1 yr time scales. The entire optical/UV continuum rises and falls almost simultaneously, so that the logarithmic slope of the power spectrum (between -2 and -3) is nearly the same for all bands, but the flux at higher photon frequencies varies with larger amplitude. Within the context of thermal accretion disk models for the production of the UV continuum, these results lead to two important inferences: that orbital dynamics at the place where the radiation is generated do not control the dominant fluctuations; and the radial group speed of accretion disk temperature fluctuations is greater than $c/10$. A possible explanation for the near-simultaneity of fluctuations in the UV and optical bands is that much of the optical continuum is due to reprocessing by outer, cooler material of UV photons created closer in.

The emission-line response functions map the marginal emission-line emissivity onto a set of paraboloidal isodelay surfaces. Combining the response functions with photoionization models, we find that the emission-line material around this Seyfert nucleus may best be described by a highly ionized inner zone of high and nearly constant pressure ($nT \sim 10^{15}$ K cm^{-3}) that stretches from $\simeq 4 - 14$ lt-days from the center, and an outer, more weakly ionized zone of considerably lower ionization at least $\simeq 20$–30 lt-days out. Both zones are suggested by photoionization models of the mean line ratios. While the inner region is probably roughly spherical, there are indications that the outer region is flattened. It is possible that the low-ionization region forms a ringlike structure of radius ~ 100 lt-day which is roughly edge-on to the line of sight. Most of the mass in the emission-line region is in the low-ionization portion, but the bulk of the line luminosity (excluding Fe II) comes from the high-ionization part.

The dispersion in line-of-sight velocity for each line is well correlated with the lag at which the cross-correlation function with respect to the UV continuum peaks: $\sigma \propto \tau_l^{-0.51}$. Such a correlation is consistent with the view that gravity is responsible for the motions of the line-emitting material if the central mass is $\sim 10^7$–$10^8\ M_\odot$; this mass range is (barely) consistent with the mass estimated on the basis of the accretion disk spectral fit.

Subject headings: galaxies: individual (NGC 5548) — galaxies: nuclei — galaxies: Seyfert — line profiles — radiation mechanisms — ultraviolet: spectra

1. INTRODUCTION: THE NGC 5548 CAMPAIGN

Variability has long been a hallmark of active galactic nuclei, but its systematic study began only in recent years. These efforts have focused on two problems: the character of continuum variability, in the hope that this will shed light on the dynamics of the continuum-producing region; and relating emission-line variations to continuum variations, in the hope that this will inform us about the geometry of the line-emitting region. In the absence of submicroarcsecond imaging, variability studies are almost the only technique available for the latter task. Unfortunately, most monitoring efforts to date have lacked sufficient duration, density, or uniformity of sampling to permit much progress on these programs. The best quality data has been obtained for studies of the X-ray continuum: *EXOSAT* observed a number of Seyfert galaxies long enough to measure the fluctuation power spectrum in the 2–10 keV band from time scales $\simeq 15$ minutes to $\simeq 24$ hr (Lawrence et al. 1987; McHardy & Czerny 1987).

Because active galaxy light curves are in general highly irregular, any investigation of AGN variability must be statistical. This means, of course, that large numbers of observations are required. It also means that choosing appropriate sampling is critical. The interval between observations must be short enough to resolve the fluctuations of interest. In addition, it is of great advantage for the sampling to be done at equal intervals. Finally, it is important to observe a continuum band as close in energy as possible to the actual band responsible for driving the lines if one wishes to relate emission lines to the ionizing continuum which powers them.

It was with these desiderata in mind that a large consortium undertook a campaign to monitor the ultraviolet flux of a particular Seyfert galaxy, NGC 5548, with sufficient intensity, duration, and regularity to permit a detailed analysis of its variability. As described in Clavel et al. (1990), spectra were taken with the *International Ultraviolet Explorer* (*IUE*) using both the LWP and SWP cameras at 60 epochs spaced very nearly 4 days apart. Happily, the fluctuations observed, both in the continuum and in many of the lines, were large compared to the measurement error, and permit extensive analysis.

In this paper we use the data from this monitoring campaign both to analyze the continuum variability properties of this Seyfert galaxy and to derive the structure of its emission-line region. We begin by discussing how the particular observing strategy chosen influences what analysis can be done (§ 2). We then set the stage for what follows by discussing the mean properties of NGC 5548 as revealed by this experiment (§ 3). Next we move on to present the inferences that can be made from continuum variability (§ 4) and line variability (§ 5). In § 6 we combine the emission-line response functions obtained in § 5 with photoionization modeling to produce a geometrical model for the broad emission-line region in this Seyfert galaxy. Finally in § 7 we summarize our principal conclusions.

2. OBSERVING STRATEGY

NGC 5548 was chosen primarily because it is bright in the ultraviolet (as well as at other wavelengths), and had well-documented large amplitude line and continuum variability (Peterson et al. 1990; Rosenblatt & Malkan 1990; Wamsteker et al. 1990). In addition, the relative blueness of NGC 5548's far-infrared–ultraviolet spectral energy distribution (Edelson & Malkan 1986) and lack of internal soft–X-ray absorption indicates that our line of sight to the nucleus is essentially unobscured. It also ensures that stellar light contamination of the ultraviolet continuum is very small. For example, using either the McAlary & Rieke (1988) or Malkan & Filippenko (1983) estimates of visual starlight flux and a standard galaxian spectrum, one finds that no more than 5% of the total 2625 Å flux observed by *IUE* at *minimum* light is from stars. Thus, even if the stars in NGC 5548 were substantially bluer than the old stellar population used by those authors, the corrections to isolate the nuclear spectrum in the UV would still be very small.

The spectra were taken regularly because regularly sampled data make the analysis much clearer and easier. Any measured Fourier transform is a convolution of the true transform with the transform of the sampling pattern's window function. When the sampling is done at regular intervals Δt and extends over a total duration T, the magnitude of the transform of the window function falls rapidly away from zero frequency [up to the Nyquist frequency $1/(2\,\Delta t]$, and is identically zero at multiples of $1/T$. On the other hand, when the sampling is irregular, the amplitude of the transform of the window function remains comparable to the amplitude at zero frequency over a wide range of frequencies. Such a broad function convolved with another smoothly varying function (the signal's true Fourier transform) leads to an irretrievable loss of information. Techniques exist for salvaging some information in the frequency domain from irregularly sampled data (Scargle 1982; Roberts, Lehár, & Dreher 1987), but they work best when the signal is periodic (i.e., has a sharply peaked Fourier transform), which does not seem to be the case for AGNs. Consequently, the NGC 5548 data set is uniquely valuable in the field of AGN variability studies, and far more information can be derived from it than from any previously available.

3. MEAN CONTINUUM AND LINE PROPERTIES

Before discussing what can be learned from variations, we prepare the ground by discussing the character of the mean continuum and line radiation.

3.1. *The Shape of the Mean Continuum*

3.1.1. *Data*

The best observational constraint on the shape of the ionizing continuum comes from simultaneous optical/UV/soft X-ray observations. Unfortunately, the shortest time gap between UV and publicly available X-ray observations of NGC 5548 was 42 days, from 1984 May 2 *IUE* observations to 1984 July 12 *EXOSAT* observations by Turner & Pounds (1989). Clavel et al. (1990) found that the autocorrelation of the UV continuum is $\simeq -0.2$ at separations around 40 days, so little correlation can be expected between the UV continuum level on May 21 and that on July 12. In order to piece together an approximation to the overall ionizing spectrum, we try instead to find spectra that lie near the historic mean levels in their respective bands, and hope that this is a fair indication of the mean continuum shape.

With respect to other X-ray observations, 1984 12 July does in fact seem to lie near the historic mean as defined by all 11 *EXOSAT* observations (taken from the *EXOSAT* Online Database at NASA/GSFC). The standard deviation of the count rates in those observations is 39% of the mean; the 1984 July 12 count rate was 10% below the mean. The NGC 5548 X-ray spectrum on that date, like that of many Seyfert 1 nuclei, was relatively flat above 1 keV ($F_\nu \propto \nu^{-0.6}$), with a "soft X-ray

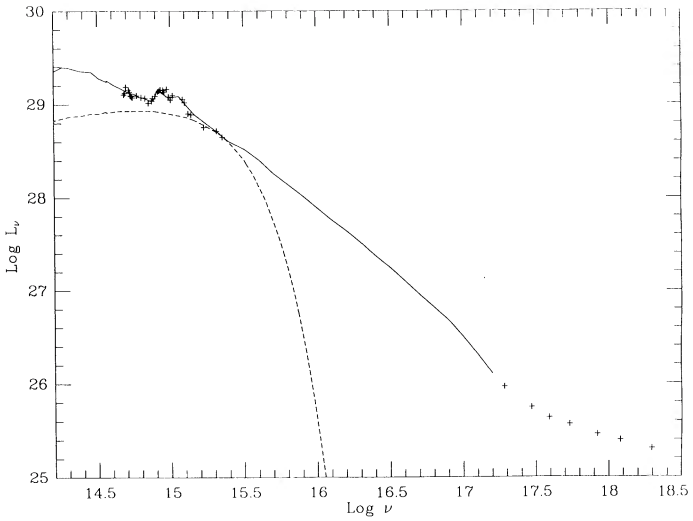

FIG. 1.—Multiwavelength continuum spectrum of NGC 5548. The plus signs are the observations described in the text. The dashed line is the best-fit accretion disk model. The solid line is our best estimate of the true continuum spectrum. At frequencies above the Lyman edge it is the "hardest plausible" spectrum as described in the text; below the Lyman edge it is the sum of the best-fit accretion disk model, a galaxy spectrum, Balmer continuum, and Fe II quasi-continuum emission. The luminosity normalization assumes $h = \frac{1}{2}$. The units of L_ν are ergs s^{-1} Hz^{-1}; the units of ν are Hz.

excess" below 1 keV (Turner & Pounds 1989). To mock up our approximate mean spectrum in the UV, we use the average of 20 "intermediate state" observations taken during the present monitoring experiment (i.e. the ones closest to the mean 1337 Å flux of 2.7 mJy). Finally, for the optical continuum, we use spectrophotometry obtained with the Steward 90 inch (2.3 m) telescope on 1984 June 6, when the continuum level was intermediate between the brightest and faintest optical spectra we have. This "average brightness level" spectrum is plotted in Figure 1.

3.1.2. *Phenomenological Interpolation*

The figure reveals a large gap across the EUV of almost two orders of magnitude in frequency in our measurements of the ionizing continuum. To construct realistic photoionization models for the BLR we must make some informed guesses about the continuum shape in this unobserved wavelength region. The procedure we adopted was to fit a smooth curve in log–log space whose EUV shape was as hard as possible. Experimentation with photoionization models using other EUV continuum shapes convinced us that this "hardest plausible" criterion was desirable.

Specifically, we constrained the EUV continuum to go through the last observed UV point, $L_\nu = 10^{28.1}h^{-2}$ at $\nu = 10^{15.35}$ (we adopt the usual abbreviation for the Hubble constant: $H_0 = 100h$ km s^{-1} Mpc^{-1}). The local slope, measured from wavelengths just longward of this point, is about -1.2, similar to the average seen in quasars (Malkan 1988). We know that the continuum slope must steepen significantly by the soft X-ray region, since the *average* UV to soft X-ray slope is -1.5. We assumed that the steepening is *monotonic*—that is, that there is no inflection point in the unobserved extreme UV continuum. Thus the EUV continuum slope must always be -1.2 or steeper. The maximum hard photon flux results from prolonging this relatively flat slope to the highest possible frequencies. To accomplish this with an analytic form, we imposed an exponential high-frequency cutoff. The cutoff frequency is set by the requirement that the continuum reach the first observed soft X-ray flux point ($L_\nu = 10^{25.33}h^{-2}$ at $\nu = 10^{17.28}$). Thus the formula which describes the ionizing continuum under these assumptions is

$$L_\nu(\text{hard}) = 10^{28.1}h^{-2} \times (\nu/10^{15.35})^{-1.2} \exp(-\nu/10^{17.26}). \quad (3.1)$$

This is our best guess of the continuum shape below Lyα.

3.1.3. *Accretion Disk Model Fit*

The model of an optically thick, geometrically thin accretion disk has had demonstrated success in describing the UV continua of quasars and Seyfert 1 nuclei. We fitted such a model to these data, assuming, in the absence of better information, a face-on disk surrounding a rapidly rotating (extreme-Kerr) black hole. The spectrum of this disk was assumed to be a sum of local blackbodies. In their 1989 paper, Sun and Malkan fitted such a model, plus additional components accounting for Balmer continuum and Fe II quasi-continuum emission, to an earlier observation of NGC 5548, from Edelson & Malkan (1986). Under the same assumptions, our best-fitting black hole mass is $1 \times 10^8 h^{-1}$ $M_\odot$, and our best fitting accretion rate is $0.004h^{-2}$ $M_\odot$ yr^{-1}. The accretion in this system is clearly very sub-Eddington: $L/L_E = 0.0045h^{-1}$ (assuming a radiative efficiency of 0.3). These parameters are very insensitive to the specific choices made for the strength and shape of the Balmer continuum and Fe II merged line emission. The fit is shown in Figure 1.

The uncertainty in our estimate of the mass comes from four sources: the width of the "valley" in χ^2-space, the unknown inclination angle, the unknown contribution to the visual flux from an infrared power law, and systematic effects due to physics unincorporated in the Sun and Malkan model. The first contribution to the uncertainty is rather small: changes of more than 30% in the black hole mass would lead to unacceptable fits. However, the contribution due to the inclination angle is significant. Sun & Malkan (1989) showed that every decrease of 0.25 in cos i leads to an approximate doubling of the best-fit black hole mass, while the physical accretion rate remains essentially unchanged. This means that our estimate of the black hole mass is a lower bound with respect to changes in inclination angle, and the upper bound might be as much as an order of magnitude larger. It is possible that a power-law component, independent of the accretion disk, may produce a substantial portion of the optical flux (see Malkan & Sargent 1982). Our fit assumed no such contribution, consistent with the hypothesis that the infrared is produced thermally, and therefore falls exponentially in the visual band. Had we included significant optical flux from an extrapolated infrared power law, the fitted black hole mass would have decreased, to cut the accretion disk's production of optical flux. The largest permissible contribution by such a power law to the optical flux corresponds to a black hole mass of $3.5 \times 10^7 h^{-1}$ $M_\odot$. Models with an even smaller black hole and more power law would fail to match the relatively flat slope of the nonstellar continuum in the optical. Without introducing specific alternative models, there is no way to be quantitative about how much the mass might change due to physics not included in our model.

This simple model does not provide an adequate description of the ionizing continuum in the soft X-ray band. The

maximum temperature in our disk model, reached near the inner radius, is only 1.0×10^5 K. Therefore, its flux drops to a negligible level by $\nu = 10^{16.5}$ Hz, well below the "soft X-ray excess." In principle, it might be possible to construct an accretion disk model with a high enough interior temperature to produce the observed soft X-ray flux. However, to do so requires having an accretion rate comparable to the Eddington limit, and the spectra from such disks generically have much harder UV continua than is the case for NGC 5548 (Madau 1988). A more likely solution to the problem of producing the soft X-ray flux arises from the fact that our principal simplifying assumption, that the disk surface emits a blackbody spectrum at the local effective temperature, breaks down at small radii. The actual spectrum could be much harder than a local blackbody, due to the modifying effects of electron scattering and Comptonization (Czerny & Elvis 1987; Wandel & Petrosian 1988). These effects can modify the emergent spectrum in the innermost part of the disk, where the effective gravity is comparatively small, while the outer regions deviate very little from the blackbody form assumed by Sun and Malkan. Thus, it might be possible for one of these modified disk models to simultaneously fit the ultraviolet and soft X-ray observations with little change in the derived parameters (black hole mass and accretion rate).

3.2. *Mean Line Fluxes and Profiles*

3.2.1. *Separating Broad- and Narrow-Line Components*

Clavel et al. (1990) measured the mean fluxes of the emission lines over the 6 observations. We note that these are *total* line fluxes. The bright emission lines of Lyα, C IV λ1549, and C III] λ1909 all have clearly separable broad and narrow-line components. With the same multicomponent model and fitting technique used to derive the line fluxes in the GEX-extracted spectra of Clavel et al. (1990), we have fitted the weighted mean spectrum of these data. Details of this fitting procedure are discussed in Reichert et al. (1991). In Tables 1A–1C we list the best-fit parameters of this model for the continuum and the emission lines, and Figure 2 shows the best-fit model traced over the mean spectrum.

The error bars for the various components given in Table 1 are purely statistical, and their derivation is described in Clavel et al. (1990) and Reichert et al. (1991). Additional systematic errors due to blending and the particular choice of fitting functions may also be present. We discuss this in detail below for the Lyα line since it is crucial for evaluating photoionization models. Other badly blended lines such as He II λ1640 + O III] λ1663, Mg II λ2798, and the Fe II lines in the LWP spectrum may also have additional systematic errors in their fluxes.

TABLE 1

FITS TO MEAN SWP AND LWP SPECTRA

A. CONTINUUM PARAMETERS

Component	F_λ(1000 Å) (10^{-14} ergs cm^{-2} s^{-1} Å^{-1})	Power-Law-Index
SWP power law	5.57 ± 0.24	0.91 ± 0.07
LWP power law	6.18 ± 0.25	0.93 ± 0.10

TABLE 1B

EMISSION LINE PARAMETERS

Component	Flux (10^{-13} ergs cm^{-2} s^{-1})	V (km s^{-1})	σ (km s^{-1})
Lya 1216 broad	52.4 ± 3.4	−578 ± 73	3807 ± 48
Lya 1216 narrow	13.2 ± 1.4	+174 + 24	727 ± 24
NV λ1240	9.3 ± 1.7	+122 ± 238	4089 ± 190
O I λ1304	0.7 ± 0.3	−738 ± 362	1266 ± 226
Si IV + O IV] λ1400	5.6 ± 0.6	−502 ± 147	2127 ± 105
C IV λ1549 blue wing	2.7 ± 0.8	−1140 ± 590	3236 ± 438
C IV λ1549 broad core	43.7 ± 1.2	−684 ± 57	4549 ± 57
C IV λ1549 red wing	1.7 ± 1.0	2038 ± 952	3236 ± 590
C IV λ1549 narrow blue	6.7 ± 0.2	−2149 ± 38	1066 ± 57
C IV λ1549 narrow	13.9 ± 0.7	+591 ± 19	914 ± 19
He II 1640 + O III] λ1663	7.5 ± 1.8	+463 ± 216	3595 ± 180
C III] λ1909 broad	6.6 ± 0.5	−1213 ± 62	2517 ± 46
C III] λ1909 narrow	3.0 ± 0.3	+7 ± 31	1035 ± 31
Fe II λ2603	1.0 ± 0.4	−708 ± 443	2248 ± 261
Fe II λ2726	1.4 ± 0.3	−128 ± 151	1611 ± 119
Mg II λ2798	12.9 ± 0.4	−309 ± 21	1949 ± 21
Fe II λ2838	2.0 ± 0.3	−249 ± 104	1515 ± 83
Fe II λ2964	0.8 ± 0.4	−789 ± 469	2044 ± 389

TABLE 1C

ABSORPTION-LINE PARAMETERS

Component	τ_0	V (km s^{-1})	σ (km s^{-1})
N V absorption	5.6 ± 1.7	−1030 ± 48	999 ± 48

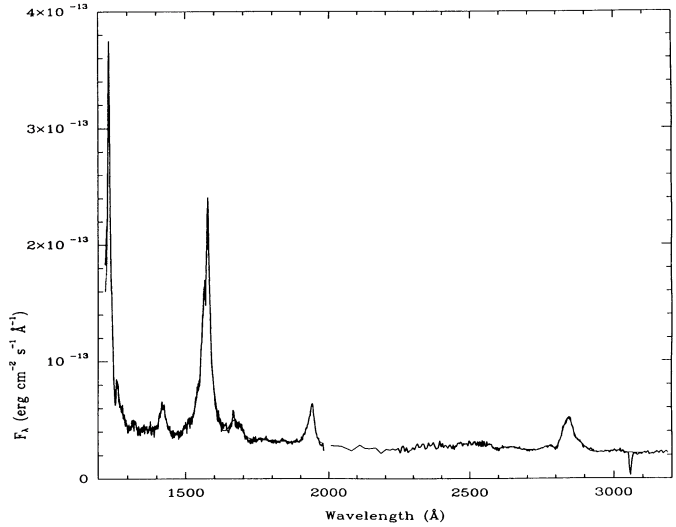

FIG. 2.—The GEX-extracted, weighted-mean spectra from the SWP and the LWP are shown for NGC 5548. The heavy solid line is the data, and the smooth light line is the best-fitting multicomponent model.

Given the good agreement, however, between the Mg II fluxes derived independently from the GEX and the SIPS data in Clavel et al. (1990), we estimate that the residual systematic error on the Mg II flux is no more than a few percent.

The line centers in Tables 1B and 1C are given as velocity offsets from the nominal line centers in the rest frame of NGC 5548 for a redshift of $cz = 5050 \pm 40$ km s^{-1} (the redshift of the narrow optical lines; Huchra 1990). The velocity of the He II + O III] blend is referenced to the He II λ1640 rest wavelength. Nearly all the broad-line components are blueshifted with respect to the systemic redshift, but by far the largest of these is the 1200 km s^{-1} offset of C III] λ1909.

The low resolution of the *IUE* spectra makes it difficult to unambiguously attach physical significance to the several components fit to the Lyα, C IV, and C III] emission lines. For example, the C IV profile has a sharp peak at the systemic redshift of NGC 5548, and a dip to the blue side of this peak. The dip could either be interpreted as an absorption component (similar to the blueshifted feature associated with N V λ1240), or a valley between a narrow-line component at the systemic redshift and an additional, blueshifted narrow-line component. While no other emission line exhibits such a double narrow peak, a model with two narrow Gaussians provides a better fit than a narrow line plus blueshifted absorption ($\Delta\chi^2_\nu = 1.86$ for 255 degrees of freedom). The narrow peak at the systemic redshift is unresolved and does not vary significantly over the course of the 60 observations; therefore, we interpret this as the narrow-line component of C IV λ1549. In contrast, the blue peak *does* vary, so we include its flux in the broad-line flux from C IV. We also include the broad Gaussians on the red and blue wings of C IV as part of the broad-line flux, but we attach no additional physical significance to either of these components. The simple two-component model which adequately fits Lyα and C III] λ1909 fails to match the higher signal-to-noise ratio C IV profile. An F-test rejects a two-component, narrow-line plus broad-line fit in favor of the five-component model at more than the 99.9% level.

The narrow Gaussians fit to the peaks of Lyα and C III] are also unresolved in the *IUE* spectra, and they do not vary significantly over the course of the 60 observation epochs (Reichert et al. 1990). We therefore interpret these narrow Gaussians as good measures of the narrow-line components of these lines. For the remaining emission lines, we see no obvious narrow-line components, but this may simply reflect the lower signal-to-noise ratio in the fainter lines.

3.2.2. *Velocity Shifts and Widths*

The narrow components of Lyα, C IV, and C III] are all within 600 km s^{-1} of the redshift given by Huchra (1990) for the narrow optical lines. Given the 2.2 Å or more uncertainty in the *IUE* wavelength scale, primarily due to target placement in the large aperture (Gass & Thompson 1985), the UV narrow-line components are at the same redshift as the optical narrow lines. The broad components of all the broad lines are blueshifted relative to the narrow-line redshift by 300–1200 km s^{-1}. This is less than the $\sim$2000 km s^{-1} offset for the variable blue component of Hβ noted by Peterson, Korista, & Cota (1987), Stirpe, de Bruyn, & van Groningen (1988), and Peterson et al. (1990).

We compare the profiles of the broad-line components of the different lines in Figure 3. We choose the C IV profile as the standard of comparison. To construct these profiles we first

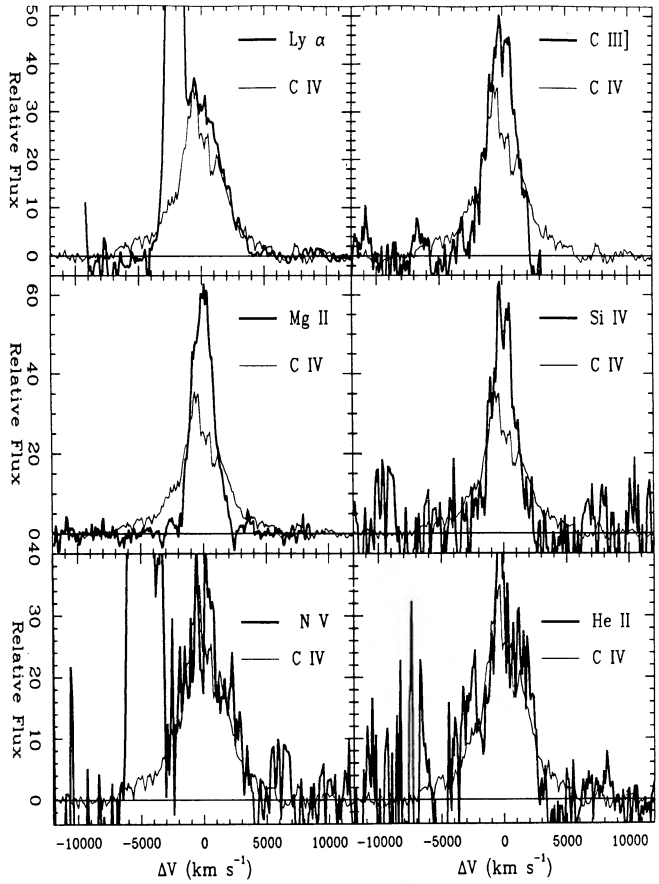

FIG. 3.—Broad-line profiles for the strongest broad lines in NGC 5548 are compared to the profile for the broad component of C IV λ1549. As indicated in the upper right corner of each panel, the heavy solid lines show the Lyα, C III], Mg II, Si IV + O IV], N V, and He II + O III] profiles. The lighter solid line in each panel is the broad component of C IV. All line profiles have been normalized to have equal area in these plots and have had narrow components removed. Note that weak lines such as Si IV are very noisy far from the line center ($\pm$5000 km s^{-1}) and have little area there since the mean flux is nearly zero.

subtracted the fitted power-law continuum from the mean spectrum. The fitted narrow-line components were then subtracted from the Lyα, C IV, and C III] profiles, and adjacent blended features were also subtracted. For example, the fitted Lyα components were subtracted to show the residual N V λ1240 line, and the C IV components have been subtracted to show the Si IV + O IV] λ1400 and the He II λ1640 + O III] λ1663 blends more clearly. We also removed the N V λ1240 absorption feature. The resulting profiles were then normalized to the total flux of the fitted broad-line components of each line, so each profile illustrated in Figure 3 has the same dimensionless area. In the figures, zero velocity is defined as the center of the broad-line profile.

While C IV, Lyα, N V λ1240, and He II λ1640 all have broad-line profiles which are basically similar, Si IV λ1400 and the lower ionization lines C III] λ1909 and Mg II λ2798 have significantly narrower profiles. This is also apparent in the dispersions of the Gaussians fitted to each of these lines given in Table 1. This trend in profile widths is anticorrelated with the peak of the delay in the cross-correlation functions (see § 5.1 below) for the same lines as illustrated in Figure 4, where σ is the Gaussian dispersion and τ is the peak delay. Possible interpretations of this correlation are discussed in § 6.4.

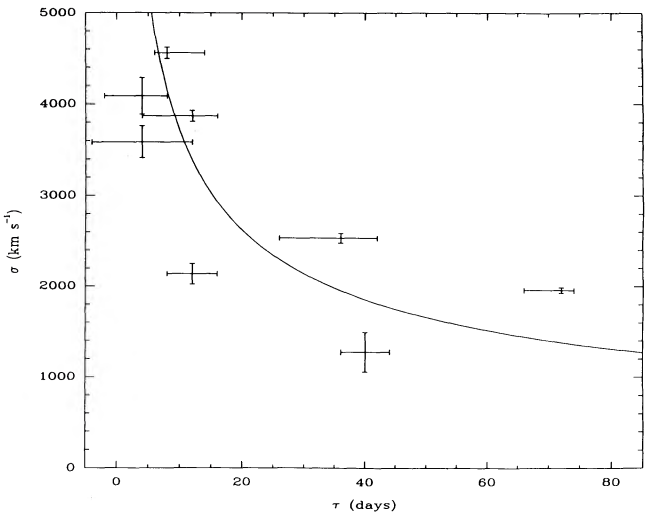

FIG. 4.—The Gaussian dispersion σ of each broad line component as given in Table 1 is plotted against the peak delay τ_l in the cross-correlation function for that line from Table 5. Error bars are 1 σ. The solid curve is a least-squares fit to the form $\sigma \propto t_l^{-1/2}$.

3.2.3. *Lyman-α*

It is harder to define the Lyα profile because the line is substantially contaminated by geocoronal emission. We discuss the issues involved in some detail because the measured Lyα flux can change substantially depending on the choices made in modeling its profile. While the narrow-line component of Lyα is well resolved from the geocoronal emission, the broad component peaks just to the red of the geocoronal emission. The total fluxes tabulated by Clavel et al. (1990) are conservative estimates that avoid any possibility of geocoronal contamination. To make a more realistic assessment of the broad-line component of the Lyα flux and evaluate the potential systematic errors, we have tried a variety of deblending procedures on the weighted-mean, GEX-extracted spectrum.

The first procedure was the one described in Clavel et al. (1990) and Reichert et al. (1990). This is called model 1 in Table 2 below, and it serves as the baseline for comparing the alternative deblending procedures. In it the Lyα region of the GEX-extracted spectra was fitted with three Gaussian components for Lyα and N V λ1240 and a single Gaussian in optical depth for the N V λ1240 absorption feature. Lyα was modeled with a narrow component at the *IUE* instrumental resolution and a single broad Gaussian. Fits were restricted to wavelengths above 1232 Å to avoid geocoronal emission. The power-law continuum was fixed by the fit to wavelengths greater than 1335 Å.

Because the GEX-extracted spectra seem to be free of geocoronal emission at wavelengths longer than 1225 Å, an alternative flux measurement is provided by extending the fitted wavelength range all the way to 1225 Å. This is model 2, and it results in slightly more flux in the broad component of Lyα. In model 3, we force the broad component of Lyα to have the same structure as the broad component of C IV λ1549, which is well described by three Gaussians—a broad core, and additional broad components on the red and blue wings. The relative widths and positions of each of these components were fixed in velocity space when fitting them to the Lyα region, but the central wavelength was permitted to vary freely. The N V λ1240 emission and absorption components were treated as before, and wavelengths above 1225 Å were fitted. The greater width and the broad low wings of the C IV profile result in even more Lyα broad-line flux and decrease the N V contribution to the blend. In model 4 we use the same C IV profile, but we force its central wavelength to have the same velocity offset from the narrow-line component of Lyα as it does in the C IV fit. As the broad red wing is moved further to the red, broad Lyα gains flux at the expense of N V λ1240. Finally in model 5 we force the Lyα profile to have the same velocity width as that of the Gaussian used to describe the broad component of C III] λ1909 (σ = 2550 km s^{-1}). This is much narrower than the core of C IV λ1549 (σ = 4560 km s^{-1}) or even the single Gaussian fit to Lyα in models 1 and 2 (σ = 3850 km s^{-1}). The fitted broad Lyα flux is very low, and N V approximately doubles in flux.

The results of each of these models are summarized in Table 2, where we give separately the fluxes of the narrow and broad components of Lyα and the flux of N V λ1240. The large

TABLE 2

FITS TO Lyα + N V λ1240

Model n	Narrow Lyα (10^{-12} ergs cm^{-2} s^{-1})	Broad Lyα (10^{-12} ergs cm^{-2} s^{-1})	N V λ1240 (10^{-12} ergs cm^{-2} s^{-1})	τ_0(N V)	χ^2	N_{pts}	N_{par}
1.....	1.32 ± 0.14	5.24 ± 0.34	0.93 ± 0.17	5.6 ± 1.7	4555	58	12
2.....	1.12 ± 0.14	6.08 ± 0.32	1.02 ± 0.18	5.5 ± 1.8	5491	64	12
3.....	1.19 ± 0.14	7.45 ± 0.38	0.74 ± 0.18	5.8 ± 1.7	5504	64	11
4.....	1.11 ± 0.14	7.69 ± 0.38	0.50 ± 0.18	6.9 ± 1.8	5694	64	10
5.....	0.90 ± 0.15	4.30 ± 0.27	1.72 ± 0.19	6.0 ± 1.8	6550	64	11

TABLE 3

ADOPTED MEAN LINE RATIOS

Emission Line	Flux Ratio to Broad C IV
Lyα b	$1.18^{+0.09}_{-0.47}$
Lyα n	0.22 ± 0.018
N V λ1240	$0.14^{+0.17}_{-0.05}$
O I λ1300	0.013 ± 0.006
Si IV+O IV] λ1400	0.10 ± 0.011
C IV λ1549 n	0.25 ± 0.015
He II λ1640+O III] λ1663	0.14 ± 0.034
C III] λ1909 b	0.12 ± 0.0095
C III] λ1909 n	0.056 ± 0.0063
Mg II λ2798	0.24 ± 0.011

NOTE.—Here "b" stands for broad, "n" stands for narrow.

reduced χ^2 for the fits reflects the fact that systematic errors such as pattern noise in the SWP camera are dominating the noise in the spectrum (Reichert et al. 1990). Thus the statistical error bars provided by GEX are a severe underestimate of the total noise in such a high signal-to-noise spectrum. Although models 2–5 all have higher values of χ^2 than model 1, an F test shows that they are all acceptable alternatives for fitting the Lyα region. At the low flux extreme of model 5, the ratio of broad C IV to broad Lyα is 1.3. At the high flux extreme represented by model 4, the C IV/Lyα ratio is 0.7. Similarly, the ratio of N V to Lyα ranges from 0.18 for model 1 to 0.06 for model 4.

3.2.4. *Measured Mean Line Flux Ratios*

In Table 3 we give the mean line ratios we adopt for our subsequent analysis. Since C IV is the best measured line, we normalize all fluxes to it. We use the mean of models 1–4 in Table 2 for our best guess at the Lyα and N V fluxes, but since systematic uncertainties in deblending these lines dominate the errors, we give errors which cover the full range of models 1–5. For the errors in the remaining line fluxes, we use the errors obtained from the error matrix of the fit scaled by the same factors applied to the GEX flux errors in Clavel et al. (1990). Note that we show no values for Fe II lines because they are so difficult to measure accurately. In this paper we are almost exclusively concerned with inferences from variability; the large uncertainties associated with the Fe II fluxes would make them almost uesless for such work.

Comparing the summed flux in all the broad lines (except Fe II) to the observed continuum flux, we find that photoionized emission line material must cover a fraction $C \geq 0.25\Omega^{-1}$ ($\lambda_c F_c/F_{\rm ion}$) of the continuum source, where Ω is the efficiency of producing emission-line energy relative to the ionizing flux incident on the material, and $\lambda_c F_c/F_{\rm ion}$ is the ratio of monochromatic flux at 1337 Å to the integrated ionizing flux. $F_c/F_{\rm ion}$ is necessarily somewhat uncertain due to our inability to directly measure the EUV spectrum. If we adopt the "hardest plausible" spectrum discussed in § 3.1, $C \geq 0.11\Omega^{-1}$. Because these estimates of the total line flux do not include the bulk of the Fe II emission, they lead to estimates of C which are really just lower bounds.

3.3. *Mean Line Flux Photoionization Models*

The traditional way of inferring the physical conditions (and distance from the central source) of emission-line material in active galactic nuclei is by comparing the observed ratios of the total line fluxes to the predictions of photoionization models. As a foil for the reverberation mapping analysis of § 5 and § 6, we have done this for these data. The code we use is the one described in Kallman & McCray (1982), Krolik & Kallman (1984), and Kallman & Krolik (1986). Its free parameters are the ionization parameter Ξ, which we define in the manner of Krolik, McKee, & Tarter (1981), $\Xi \equiv F_{\rm ion}/(cn_{\rm H}kT)$; the pressure due to hydrogen nuclei: $p \equiv n_{\rm H}kT$; the column density of emitting material N; the elemental abundances, which we took to be solar; and the shape of the ionizing spectrum.

After testing a broad range of possible EUV spectra, we concluded that for virtually any shape which connects smoothly to the observed UV and soft X-ray spectra, there is *no* single set of physical conditions (Ξ, p, N) which reproduces the ratios of Table 3. The problems are seen most clearly in terms of the carbon lines. In order to produce as much C IV λ1549 relative to Lyα as is seen, the illuminated surface of the material must be highly ionized—in this region C is mostly C IV and C V. If sufficient C III] λ1909 is to be generated by the same material, there must be a comparatively wide zone having moderate Lyman continuum optical depth in which the ionization balance shifts to C III. The breadth of this zone of intermediate ionization is controlled by the shape of the ionizing spectrum. Flat spectra (e.g., $F_\nu \propto \nu^{-1}$) broaden it, while curved spectra (e.g., the accretion disk spectra discussed in the previous subsection) lead to relatively narrow zones of intermediate ionization. Unfortunately, the flat spectra which are successful at reproducing the observed average line ratios predict soft X-ray fluxes which are substantially greater than those observed from NGC 5548 (Turner & Pounds, 1989).

To describe quantitatively how well different models do at reproducing the relative line strengths, we define a figure of merit $\Phi_1 = \Sigma_i \phi_{1i}$, where the sum is over the list of all measured mean broad-line fluxes taken in ratio to the C IV λ1549 flux.

$$\phi_{1i} = \begin{cases} \left(\dfrac{R_i^{\rm calc} - R_i^{\rm obs,max}}{R_i^{\rm obs,mean} - R_i^{\rm obs,max}}\right)^2, & \text{if } R_i^{\rm calc} > R_i^{\rm obs,max}\ ; \\ \left(\dfrac{R_i^{\rm calc} - R_i^{\rm obs,min}}{R_i^{\rm obs,mean} - R_i^{\rm obs,max}}\right)^2, & \text{if } R_i^{\rm calc} < R_i^{\rm obs,min}\ ; \\ 0\ , & \text{otherwise}\ . \end{cases} \tag{3.3}$$

In this expression R_i is the line ratio in question (e.g., C III] λ1909/C IV λ1549), and the minimum and maximum observed values correspond to one standard error from the most probable value (see Table 3). We use this somewhat idiosyncratic statistic rather than, for example, χ^2, to emphasize the fact that the errors in the line ratios are almost certainly not distributed normally.

Even the best single-zone model using the "hardest plausible" spectrum of § 3.1 produced $\Phi_1 = 6.3$. The typical residuals between the predictions of this model and the data are larger than the data values themselves. Consequently, although our statistic is not associated with a well-defined probability distribution, the results given by this single-zone model would appear to be unacceptable.

It is possible to do substantially better if we allow ourselves the freedom of two zones with different physical conditions. This choice is vindicated by the results of § 6. The best fit we found ($\Phi_1 = 0.57$) was for a model with separate high-ionization and low-ionization zones. The high-ionization component had $\Xi = 0.3$, $p = 0.3$ dyne cm^{-2}, and $N = 10^{22}$ H

cm^{-2}, while the low-ionization component had $\Xi = 0.1$, $p = 0.003$ dyne cm^{-2}, and $N = 10^{23}$ cm^{-2}. If any of these parameters is changed by more than a factor of 3 in either direction, Φ_1 rises to greater than 10.

To fit the observed line ratios, the contributions from the two zones were added with a ratio of total line fluxes, i.e., covering factors C, of 1:6, low ionization to high ionization. Note that the high-ionization zone has an implied radius 0.058 times smaller than the radius of the low-ionization zone. The total mass in each zone is $4\pi r^2 CN\mu_H$, where μ_H is the mean mass per H atom, so the low ionization zone has 500 times the mass of the high-ionization zone. Normalizing to the observed equivalent widths, the total predicted covering factor for material producing the measured lines is 0.36, corresponding to a mean $\Omega \simeq 0.3$—a large part of the incident ionizing flux either passes right through the high-ionization inner clouds, or is reradiated in the Lyman and Balmer continua.

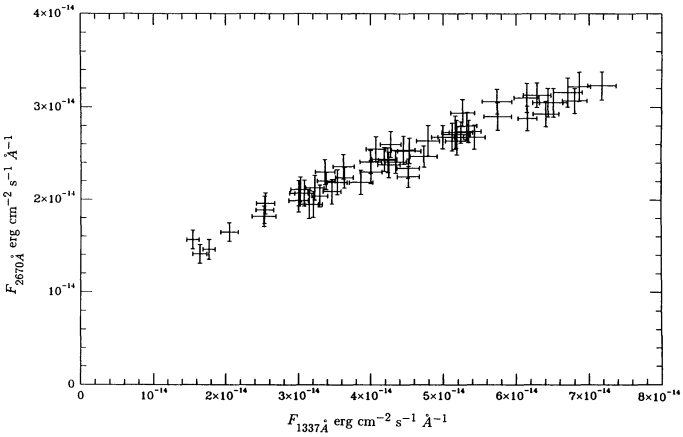

FIG. 5.—Correlation of 2670 Å continuum flux with 1337 Å continuum flux. The error bars are ± 1 σ.

4. CONTINUUM VARIABILITY

4.1. *Comparative Variability of Different Continuum Bands*

Clavel et al. (1990) showed that all three UV continuum bands and the FES (5000 Å) band varied during the 8 months of observation. In Table 4 we list the fractional fluctuation amplitudes (i.e., ratio of rms variation in flux to mean flux) in each band and demonstrate that the variations in each were very clearly statistically significant. As Clavel et al. showed, the fractional amplitude of variation increased with decreasing photon wavelength, in line with the earlier studies of this and other Seyfert galaxies by Cutri et al. (1985) and Edelson, Krolik, & Pike (1990).

Another way of viewing this effect is to look at the correlation between the flux levels in two different UV continuum bands, for example those near 1300 and 2700 Å as shown in Figure 5. There is a clear positive correlation between the two; moreover, although the correlation is close to linear, there is clear curvature in the sense that at high flux levels the flux in the longer wavelength band does not increase as rapidly as that in the shorter wavelength band. This curvature confirms the result of Edelson et al. (1990) that the ultraviolet spectra of NGC 5548 and other variable Seyfert galaxies harden as they brighten.

It is also noteworthy that the extrapolation of the trend to zero flux in the 1300 Å band appears to predict nonzero flux in the 2700 Å band. This is probably due to the presence in the 2700 Å band of significant Balmer continuum and merged Fe II emission. The contribution to the measured continuum flux due to Fe II and Balmer continuum can diminish the variability amplitude by less than linear response to continuum fluctuations in the material radiating the lines (Wamsteker et al. 1990; Clavel et al. 1990) and by time-delay smearing of rapid fluctuations (both lines are presumably radiated at large distances from the true continuum source).

One plausible interpretation of these consistent spectral changes is in terms of thermal accretion disk models. As we discussed in § 3.1, the optical/ultraviolet continuum of NGC 5548 is reasonably well described by a sum of a power law which dominates the nonstellar light in the optical, and a quasi-thermal accretion disk spectrum which dominates in the ultraviolet. If we make the supposition that only the accretion disk part varies, we find that the ratios of the observed rms fluctuations to the best-fit accretion disk flux are 0.33, 0.28, 0.27, and 0.11 for the 1300, 1850, 2700, and 5000 Å bands, respectively. Given the uncertainty in these numbers due to the uncertainty in the disk model, they are not badly described by the power law $\delta F/\bar{F}_{\rm disk} \propto \nu^{0.8}$.

TABLE 4

CONTINUUM VARIABILITY PARAMETERS

Band (Å)	$\bar{F}_c$ (10^{-14} ergs cm^{-2} s^{-1} $Å^{-1}$)	$\delta F_c/\bar{F}_c$ (%)	χ^2	p
1337.....	4.37	31.9	103.9	$<10^{-38}$
1813.....	3.33	26.2	109.3	$<10^{-38}$
2670.....	2.44	18.6	13.1	$<10^{-38}$
5000.....	50.6[a]	7.6	3.8	10^{-20}

[a] FES fluxes in uncalibrated flux units.

4.2. *Fluctuation Power Density Spectrum*

The best way to characterize the distribution of variability with time scale in chaotic sources such as AGNs is to construct the fluctuation power density spectrum (FPDS). Previous, unevenly sampled observations were not well suited for measuring the FPDS, because there is no good method for measuring the Fourier transform of an unevenly sampled data stream (§ 2). However, these evenly sampled ultraviolet data allow the first reliable measurement of the FPDS in a non–X-ray band for any active galaxy.

The FPDS for the 1337 Å band is presented in Figure 6; except for their amplitude, the FPDS for the other two UV bands are essentially indistinguishable from the one shown. We computed all three using standard techniques (e.g., Bracewell 1986) without subtracting the mean, and applying a Welch (parabolic) window to the data to de-emphasize the poorly sampled contribution of low-frequency fluctuations. The FPDS we show is normalized to the time-integrated fluence in that band. All three power spectra are well described by power laws with exponents -2 to -3 at temporal frequencies below 0.033 day^{-1} (30 days), but the uncertainty in the power spectrum at the lowest frequencies is substantial because our observations spanned only a few periods for them. This very "red" FPDS means that the variations are dominated by fluctuations on the longest time scales sampled by these data. This is also intuitively obvious from inspection of the light curves shown in Clavel et al. (1990), which showed little variation on short time

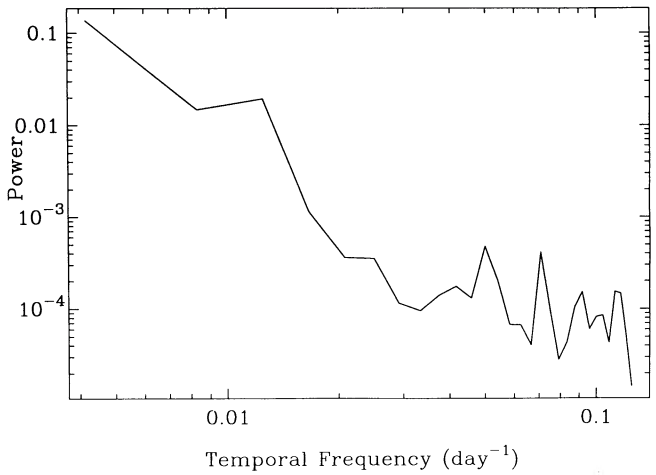

FIG. 6.—Continuum FPDS for the 1337 Å band; the other two UV bands are very similar in character. The FPDS falls steeply from $(240^d)^{-1}$ to $(30^d)^{-1}$ and can be characterized as a power law with exponent between -2 and -3. At higher temporal frequencies, this FPDS (and the other two as well) are flat in frequency due to measurement noise.

scales. If the FPDS were any steeper than this, leakage through the sidelobes of even this evenly spaced window function would artificially flatten the FPDS (Deeter & Boynton 1982).

Such a steep slope cannot continue indefinitely to lower frequencies, because the power in the FPDS would diverge. We may estimate the position of this low-frequency break by making use of the theorem that the integral of the power spectrum is equal to the variance. Over the first 11 years of operation of *IUE*, 1978–1988, the rms fractional fluctuation amplitude of NGC 5548 measured at 1450 Å was 0.32 (Edelson et al. 1990). This is almost identical to the amplitude of 1337 Å variations seen over the 8 month period measured here. In addition, the mean level of the older observations matches that during the 8 month monitoring campaign to within $\simeq 20\%$. We therefore conclude that there can be very little integrated power on time scales between 8 months and 11 years, i.e., the FPDS must flatten at frequencies not far below those which have been measured in the 8 month monitoring campaign.

At temporal frequencies above $\simeq 0.033$ day^{-1}, the FPDS is flat. The most natural interpretation of this feature is to ascribe it to uncorrelated measurement error. The integrated variance due to this component in the power spectrum gives an rms contribution to the fluctuations of $\simeq 5\%$ consistent with the measurement error estimated by Clavel et al. (1990) ($\simeq 3\%$–4%) when the effect of the Welch window is taken into account.

4.3. *Phase Information*

In principle, there is also significant information in the phase of the Fourier transform as a function of frequency. For example, if the phases appear to be uncorrelated, the fluctuations may be interpreted as Gaussian noise, suggesting a process with a large number of independently varying elements. On the other hand, if the phases are correlated, we may be able to learn something about the structure of the fluctuating region from the particular nature of the correlation.

Unfortunately, in this case there are only seven or eight frequency points for which the phase is dominated by signal rather than noise. They exhibit a weak tendency to cluster in three groups at $\sim\pi/4$, π, and slightly less than 2π, but with so few points little can be said reliably.

4.4. *Continuum Cross-Correlations*

Although the phase as a function of frequency is not very informative here, the relative phases between the different bands do give significant information. These are best explored through interband cross-correlation functions. If different bands appear uncorrelated at all lags, then we may argue that they are produced by independent mechanisms; conversely, if they are correlated but separated by a time delay, we learn about causal connections between different zones of a single radiating region.

Figure 7 shows the continuum cross-correlation functions. In all cases it is clear that the different continuum bands are very well correlated with each other. The maximum correlation in all cases is at zero lag, but the 1337–1813 Å and 1337–2670 Å cross-correlation functions show very slight evidence for skewness in the sense that the longer wavelengths lag the shorter. It is possible that higher time resolution data would show that the actual peak is slightly off zero; any such offset is certainly much less than our 4 day sampling interval. The 1337–5000 Å correlation function shows stronger skewness. The cross-correlation at a lag of $+4^d$ is only slightly smaller than the value at 0^d, so we suspect more strongly than for the shorter wavelengths that higher resolution data would detect a peak at finite lag. The 1337–5000 Å cross-correlation crosses zero at -24^d and $+34^d$, so the mean of the zero-crossings is near $+5^d$. However, it is important to note that some of this lag could be due to contamination of the FES continuum by Hβ and Fe II multiplets, whose variable flux presumably lags the ultraviolet (and soft X-ray) continuum. In sum, we regard these cross-correlations as demonstrating that all the continuum bands vary nearly synchronously, with at most a 4^d lag between the 1300 Å band and the 5000 Å band.

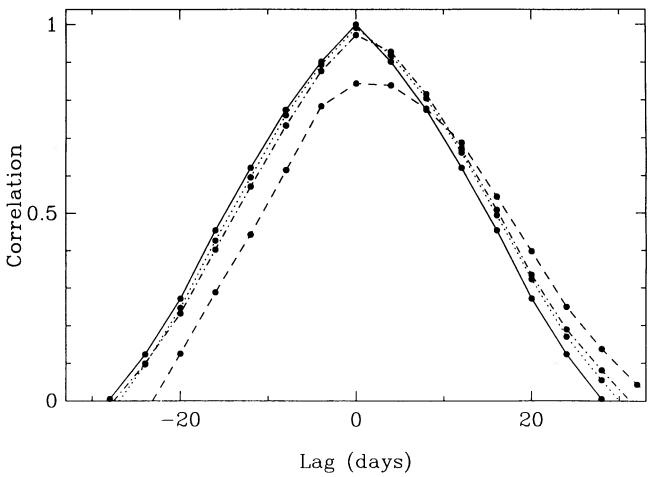

FIG. 7.—Continuum auto- and cross-correlation functions. The solid line is the 1337 Å autocorrelation function, the dotted line is the 1337–1813 Å cross-correlation function, the dot-dashed line is the 1337–2670 Å cross-correlation function, and the dashed line is the 1337–5000 Å cross-correlation function. There is a tendency for the lower-frequency variations to lag behind those at 1337 Å, but even for the 1337–5000 Å cross-correlation, which peaks near $+2$ days and crosses zero at -24^d and $+34^d$, the lag is at best marginally significant.

4.5. *Connection to Continuum Production Models*

The least model-dependent limit imposed by these data is that the continuum production region must be smaller than $\simeq 1$ lt-yr in order for fluctuations on the dominant time scale ($\simeq 1$ yr) to be causally coordinated. Similarly, the near coherence of the different bands requires that the mean distances between the fluctuation driver and the regions responsible for emitting each of the bands must be the same to within 4 lt-day. However, within the context of specific models for the continuum production, it is possible to use our results to derive much more specific consequences. The general pattern is that knowledge of the fundamental signal speed puts a limit on the size of the radiating region, while knowledge of the size of the region puts a limit on the signal speed.

4.5.1. *A Toy Model*

We will interpret these continuum variations in terms of the thermal accretion disk model. To make the connection quantitative, we adopt a simple model for accretion disk fluctuations. Suppose that the local surface brightness is given by

$$S_\nu = \left(\frac{h\nu^3}{c^2}\right)\left(\frac{h\nu}{kT}\right)^q\left[\exp\left(\frac{h\nu}{kT}\right) - 1\right]^{-1}, \qquad (4.1)$$

i.e., a blackbody modified by the factor $(h\nu/kT)^q$. With this form for the emissivity, the temperature in the equilibrium disk falls with radius in the standard way, $T \propto r^{-3/4}$. Let the fluctuations take the form of local temperature fluctuations with a single frequency ω at each radius:

$$\frac{\delta T}{T} = \epsilon\left(\frac{r}{r_g}\right)^{-\beta}\exp\left[-i\omega_g\left(\frac{r}{r_g}\right)^{-\gamma}t + i\phi(r)\right], \qquad (4.2)$$

where the power laws are extrapolated to r_g, the gravitational radius of the central black hole, in order to provide a fiducial point. In this expression we have assumed that the amplitude of fluctuations and the local frequency both scale as power laws in radius. The former assumption is purely a convenience; the latter is very physically plausible because most dynamical quantities (e.g., orbital period, cooling time, etc.) scale as power laws in radius. In the limit that the fluctuations are totally incoherent, the phase is a random function of radius; in the limit that a single dispersive wave accounts for the fluctuations, $\phi = \int k_r\, dr$, where k_r is the wave's radial wavenumber. The principal restriction here is that we make no allowance for any harmonic content to the fluctuations.

The power spectrum produced in such a model is

$$\frac{|\delta\hat{L}_\nu|^2}{L_\nu^2} = \left[\frac{(5+3q)(1-q)}{4\gamma\omega_g}\right]^2\left(\frac{h\nu}{kT_g}\right)^{2(q+1)}\left(\frac{\omega}{\omega_g}\right)^{[2(\beta-\gamma)-3(q+1)/2]/\gamma}, \qquad (4.3)$$

where $(\nu/\nu_{\max})^{4\gamma/3} < \omega/\omega_g < 1$. In this last expression $\nu_{\max}$ is the highest photon frequency efficiently radiated in the disk. A power-law power spectrum in ω is naturally produced because the local oscillation frequencies are power laws in radius, and a wide range of radii contributes radiation in each photon frequency. The upper limit $\omega_{\max}$ on the range of the power law is the oscillation frequency at the innermost ring of the accretion disk; the lower limit $\omega_{\min}(\nu)$ is the oscillation frequency at the outermost ring hot enough to efficiently radiate photons of frequency ν. Thus, the higher the photon frequency, the narrower the range in ω over which we might expect to see this power law. For our highest frequency band (1337 A), the expected dynamic range $\omega_{\max}/\omega_{\min}$ is only $\simeq 2.5^{4\gamma/3}$ if the temperature at the innermost ring is the 1.0×10^5 K suggested by the spectral fit.

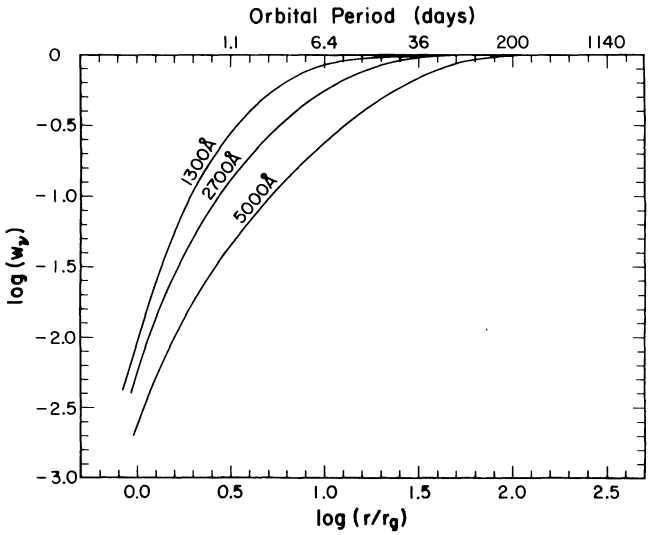

FIG. 8.—The fraction of the flux in three continuum bands radiated interior to a given radius according to our standard accretion disk model for NGC 5548 (the particular values assume $h = \frac{1}{2}$). For reference, the orbital periods for these values of r are shown along the top of the figure. The top curve refers to flux observed at 1300 Å, the middle curve refers to flux at 2625 Å, while the lowest curve shows flux at 5000 Å.

4.5.2. *Inferences from the Range and Shape of the FPDS*

Comparison of this simple model of disk fluctuations to the measured FPDS for NGC 5548 indicates that, in contrast to the common assumption, orbital dynamics do not control the fluctuation frequencies. To demonstrate this, we first estimate the orbital frequencies in the portion of the disk responsible for the UV continuum. Figure 8 shows quantitatively how the luminosity in each continuum band grows as larger radii are included. The disk model assumed is the same one identified in § 3.1. As expected, the curves showing flux at the shorter wavelengths rise faster, since the flux is more centrally concentrated to the inner, hotter rings of the disk. The orbital frequency at the radius within which half the 1300 Å flux is made is $\simeq (2^d3)^{-1}$; in contrast, the observed $\omega_{\min}$ is $\lesssim (240^d)^{-1}$. Thus, the orbital dynamics model predicts a value of $\omega_{\min}$ which is too large by more than ~ 100. This conclusion is strengthened by its insensitivity to the uncertainty in black hole mass. Within the framework of the simplest accretion disk model (local blackbody emission), the orbital frequency at the ring producing most of the flux in a given band is actually *independent* of central mass.

Two other explanations for the underlying dynamics driving these fluctuations are consistent with the measured FPDS. In the first, the accretion rate is modulated by some process in the vicinity of $r \lesssim 150 r_g = 3.4$ lt-day, where the orbital period is ~ 1 yr. This creates the power at the observed $\omega_{\min}$, while some unspecified nonlinearity in the system creates the power-law power spectrum at higher frequencies as the accretion rate disturbance propagates inward (this picture breaks the assumptions embodied in eq. [4.2] by permitting harmonics). The second suggests that the fluctuations are driven by disk

cooling. For an optically thick "α"-disk (as described, e.g., in the review by Pringle 1981), the cooling time scale is $\sim\alpha^{-1}\times$ the orbital period, so this explanation would require $\alpha\sim 10^{-2}$ for the accretion disk in this object.

When considering the logarithmic slope of the power spectra, one might start by taking the simplest model, in which $q=0$ (pure local blackbody emission), and $\gamma=3/2$ (frequencies dominated either by orbital motions or, as is more likely here, by thermal effects if the local α is constant in radius). In that case, the power spectrum is predicted to have a logarithmic slope $4\beta/3-3$. Comparing this to the measured slope of between -2 and -3 suggests that, in this simplest model, $0<\beta<\frac{3}{4}$. The dynamic range in frequency over which this power-law power spectrum would apply for the 1300 Å band would be a factor of $\simeq 6$; compared to the observed dynamic range of at least $\simeq 8$, this suggests that $\omega_{\max}$ must be near the frequency at which our observations were overwhelmed by noise, or else $\gamma>3/2$.

4.5.3. *Scaling of Fluctuation Amplitude with Photon Frequency*

This model of locally controlled fluctuations in an accretion disk also predicts a characteristic scaling of rms fractional fluctuation amplitude with photon frequency. Using the theorem that the integral over frequency of the power spectrum is equal to the integral of the variance over time, we find

$$\left\langle \frac{\delta L_\nu}{L_\nu}\right\rangle = \epsilon\,\frac{(5+3q)\,|\,1-q\,|}{8\beta-6(q+1)-4\gamma}\,(\omega_g T)^{-1/2}\left(\frac{h\nu}{kT_g}\right)^{q+1} \times\,|\,1-(\omega_g T)^{4[\gamma-2\beta+3(q+1)/2]/3}\,|^{1/2}\,. \tag{4.4}$$

Here we have used the empirical fact that, for all the continuum bands, the power laws in fluctuation frequency extend down to the lowest frequency studied, $1/T$. If $\langle\delta L_\nu/L_\nu\rangle$ scales $\propto\nu^{0.8}$ (§ 3.1), then $q\simeq -0.2$; i.e., the local backbody approximation is not too bad. For example, if the fluctuations really are regulated by local disk cooling and the α parameter is constant with radius, this value of q would alter the suggested value for β found in the previous paragraph to $-0.15<\beta<0.6$.

4.5.4. *Interband Correlations*

The near coherence between the fluctuations in all the different bands requires good phase coherence between fluctuations at different radii. In fact, in the context of an accretion disk model, the upper bound on any interband lags may be used to put a lower bound on the radial group speed of any traveling wave associated with these fluctuations. Our argument is based on the fact that most of the luminosity in any given band is radiated by the largest radius region in the disk hot enough to radiate it efficiently. Thus, substantial amplitude fluctuations like the ones observed must involve a significant part of the total area radiating that band.

Figure 8 may be used to make this argument quantitative (N.B.: it is drawn assuming $h=\frac{1}{2}$). Its vertical axis is w_ν, the fraction of total flux at frequency ν radiated inside a given radius, and may be considered also the maximum fractional amplitude of variability that could ever be observed from changes within a given radius. (The actual amplitudes ought to be smaller, since such an extreme case—the flux from the entire inner part of the disk disappearing—does not seem realistic). In the longest wavelength UV band (2700 Å), the lowest observed flux was 39% below the mean, corresponding to a minimum radius involved in the fluctuation of $8r_g=0.18$ lt day. If the lag between the innermost region and this radius is at most 2[d] (see Fig. 7), the radial group velocity must be at least $0.09c$!

Although this limit is somewhat model-dependent, within the confines of the simple accretion disk model it is only weakly dependent on uncertain parameters. The radius within which most of the flux in a given band is produced scales as the $\frac{1}{3}$ power of the central mass, so even the fact of 10 uncertainty due to the inclination angle would result in only a factor of 2 change in this lower bound on the signal speed. In fact, because inclination changes *increase* the central mass, this limit would be strengthened by other than face-on inclination.

Such a large group velocity rules out many possible sorts of waves for transmitting the fluctuation information. In any model for the central engine of this AGN which involves accretion onto a black hole and thermal production of the UV continuum, the maximum gas temperature is only $\sim 10^5$ K, so the sound speed corresponding to gas pressure-mediated disturbances is far too slow. Sound waves can be responsible only if the disk is sufficiently dominated by radiation pressure to make its thickness $h_d\gtrsim 0.36r$ at $r\simeq 8r_g$, a configuration only achievable when the accretion rate is comparable to the Eddington rate. Similar constraints apply to Alfvén waves if the magnetic pressure is limited by the gas pressure.

One of the few ways to achieve such a high group speed is for the wave to be carried by photons. Reprocessing in the outer disk of hard photons from the inner disk might well be the explanation for the coordinated optical/UV fluctuations. In that case, the signal speed argument must be revised because more of a given band's luminosity may be radiated inside a particular radius. Because the local bolometric surface brightness is $\propto T^4$ even for nonzero q, the increase in effective temperature at a radius near which a fraction dg of the intrinsic luminosity fluctuation δL is reprocessed is

$$\frac{\delta T}{T}=\frac{1}{4}\,\frac{\delta L}{dL/dr}\,\frac{dg}{dr}\,, \tag{4.5}$$

where the luminosity radiated inside radius r is $L(r)$. For a significant increase in the luminosity of photons with frequency ν, r must be restricted to the range in which $h\nu\gtrsim kT$ [i.e., $r<r_{\max}(\nu)$], so the fractional increase in the luminosity is

$$\frac{\delta L_\nu}{L_\nu}=\frac{1}{4}\int^{r_{\max}(\nu)} dr\,\frac{\delta L}{dL/dr}\,\frac{dg}{dr}\,\frac{dw_\nu}{dr}\,, \tag{4.6}$$

where $w_\nu(r)$ is the fraction of the luminosity in frequency ν radiated interior to r. To find the new lower limit on the signal propagation speed (which might in principle be smaller than c if the intrinsic radiation must diffuse out through a scattering region to reach the reprocessing site), we assume that $dg/d\ln r\leq 0.5$ and $\delta L/L_{\rm bol}\leq 1$. Reference to the curves of Figure 8 shows that the lower bound on the radial group velocity may then be reduced by a factor of 2 or so, but no more than that. A smaller maximum $dg/d\ln r$ would lead to an even smaller change in the lower bound on the radial group velocity.

5. LINE VARIABILITY

Throughout this paper, we assume that the emission lines are generated by the absorption of ionizing radiation from the nucleus (Osterbrock & Parker 1964; Bahcall & Kozlovsky 1969; reviewed by Davidson & Netzer 1979). In the conditions

that have been inferred for the line-emitting regions (e.g., Kwan & Krolik 1981), the recombination and cooling times are very short ($\gtrsim 1$ hr) compared to the light travel time from the nucleus (roughly days to months). Thus, the line flux we see today reflects a peculiar average over the continuum flux for the past several days to months. When the continuum flux varies over a wide dynamic range, the relationship between line flux and continuum flux can be strongly nonlinear; however, for small fluctuations about a mean level, we can describe the *change* in the line flux as approximately linear. That is, the local line surface brightness S_l of a photoionized region responds to changes in the local ionizing continuum flux $F_{\rm ion}$ according to

$$\frac{\delta S_l}{S_l} \simeq \frac{\partial \ln S_l}{\partial \ln F_{\rm ion}} \left(\frac{\delta F_{\rm ion}}{F_{\rm ion}} \right) \equiv \eta \left(\frac{\delta F_{\rm ion}}{F_{\rm ion}} \right) . \tag{5.1}$$

In most circumstances, η lies between 0.2 and 2. Most lines are emitted with greater power as the continuum flux rises, but the shift in ionization equilibrium and the Boltzmann factor present in all the collisional excitation rates introduce considerable deviation from strict linearity in virtually all lines but Lyα when viewed across a wide enough dynamic range in continuum flux.

The line flux F_l we observe at time t may be related to the observed continuum flux F_c at past times by

$$F_c(t) = \bar{F}_l + \int d\tau \, \Psi_l(\tau)[F_c(t-\tau) - \bar{F}_c] \tag{5.2}$$

when four conditions are satisfied: the fluctuations are in the linear regime (i.e., eq. [5.1] is appropriate); the fluctuations in all relevant continuum bands are perfectly correlated (so that F_c/F_λ is constant in time at all wavelengths λ shortward of 912 Å); the fluctuations in the continuum radiated in all directions which strike line-emitting material are perfectly correlated; and the time scale on which the structure of the emitting region changes is longer than the range of times for which Ψ is significantly nonzero.

We call $\Psi_l(\tau)$ the "response function"; it is the integral over the surface of constant delay τ of the partial derivative of the local line emissivity with respect to continuum fluctuations. Its dependence on τ gives a partial description of the geometrical distribution of line-emitting material with respect to the continuum source. Blandford & McKee (1982) pointed out that the convolution in equation (5.2) could be inverted by Fourier transforms:

$$\Psi_l(\tau) = \int df \exp(-2\pi i f \tau) \frac{\hat{F}_l(f)}{\hat{F}_c(f)} , \tag{5.3}$$

where the circumflex denotes the Fourier transform taken after subtracting off the mean. However, they astutely commented that this inversion required very high quality data and excellent time sampling. Because of these stringent requirements on data quality, weaker, but more robust measures of the emission-line gometry have been studied. We consider these first.

5.1. *Correlation Analysis*

The simplest description of the mutual relationship between line and continuum variations is the cross-correlation function:

$$C_{lc}(\tau) = \frac{1}{\sigma_l \sigma_c T} \int dt [F_l(t) - \bar{F}_l][F_c(t-\tau) - \bar{F}_c] , \tag{5.4}$$

where $\sigma_{l,c}$ are the standard deviations of the observed line and continuum fluxes $F_{l,c}$ about their means $\bar{F}_{l,c}$. If the line emission can be described by a simple linear convolution between past continuum fluctuations and a response function $\Psi_l(\tau)$, the cross-correlation is the convolution of the continuum autocorrelation with $\Psi_l(\tau)$. Consequently, the cross-correlation function is always at least as broad as the continuum autocorrelation, but its peak is shifted to positive lags because Ψ_l must be zero for $\tau < 0$. The amplitude of the peak can be reduced considerably below unity if the response function is broader than the autocorrelation function or if the signal-to-noise ratio is small. On the other hand, if the response function is narrower than the autocorrelation function, the cross-correlation function should look very much like the autocorrelation function, but shifted by an amount equal to the mean intrinsic lag. Thus, the interpretation of cross-correlation functions depends on the match between the breadth of the response function and the breadth of the continuum autocorrelation. In particular, the peak may be difficult to identify if the continuum power spectrum is very steep so that its autocorrelation is very broad. In such cases it is sometimes advantageous to measure the width of the cross-correlation and compare it to the width of the continuum autocorrelation instead of finding the position of the peak (see Edelson & Krolik 1988).

Because the 1337 Å band is the nearest of the three continuum bands to the ionizing continuum which powers the lines, we use it to describe the overall continuum variability. Clavel et al. (1990) presented cross-correlation curves for all the measured lines with respect to this continuum band. We have recalculated these using only the broad components; the results are given in Table 5. All the shapes of the cross-correlation functions (except for Mg II λ2800) are very similar and do indeed resemble the shape of the continuum autocorrelation. We immediately infer that for most of the lines (with the possible exceptions of C III] λ1909, Mg II λ2800, and O I λ1304), the characteristic delay time scales are smaller than the FWHM of the continuum autocorrelation, $\simeq 32$ days.

TABLE 5

LINE-CONTINUUM CROSS-CORRELATIONS

Line	τ_l	$C(\tau_l)$	FWHM
N V λ1240	4^{+4}_{-6}	0.79	34[d]
He II λ1640	4 ± 8	0.67	40
C IV λ1549	8^{+6}_{-2}	0.66	38
Lyα	12^{+4}_{-8}	0.84	34
Si IV λ1400	12 ± 4	0.61	36
C III] λ1909	36^{+6}_{-10}	0.56	40
O I λ1304	40^{+12}_{-24}	0.57	42
Mg II λ2800	72^{+2}_{-6}	0.46	30

NOTES.—The cross-correlation for line l peaks at τ_l with amplitude $C(\tau_l)$. The error range is determined by the place at which the estimate of the cross-correlation falls 1 σ (in the cross-correlation function) below the peak value. In both the error range and the FWHM the curves were interpolated to 2^d.

We note, however, that caution must be used before ascribing too much significance to the particular values of the lag at which the cross-correlation function is a maximum. That lag is determined by a peculiar weighted average of delay times with numerous physical and statistical biases (e.g., as discussed in Edelson & Krolik 1988). There is also a special one which operates here due to the extreme steepness of the continuum power spectrum. When that is the case, long-term trends dominate the character of the variability, and these lead to spuriously small lags for the cross-correlation peaks because nearly linear curves line up best at zero lag. We have done simulations showing that the bias due to this effect is often in the range of a factor of 2. Fortunately, the data acquired in this experiment is of such high quality that more powerful methods than cross-correlation analysis can be used, and our inferences about the geometry of the broad-line region will be almost entirely independent of cross-correlations.

5.2. *Relative Fractional Amplitudes*

Another robust diagnostic of the conditions in the line-emitting gas is the ratio, for each line, of the line fluctuation amplitude to the fluctuation amplitude of the continuum. This ratio is controlled by two effects: the sensitivity of the line's emissivity to changes in the continuum flux and the degree to which rapid continuum fluctuations are washed out by the range of delay times in the line-emitting region. In addition, each fractional fluctuation amplitude has a contribution from measurement error. The cross-correlation analysis of the preceding subsection demonstrates that in these data most of the continuum fluctuation power is on time scales very long compared to the range of delay times, so we expect the fluctuation smearing effect to be weak in all the lines except possibly Mg II λ2800 and O I λ1304.

Clavel et al. (1990) tabulated the rms fractional fluctuation amplitude of each line and continuum band. In column (1) of Table 6 we show the ratios of this quantity for each line to the rms fractional amplitude in the 1337 Å continuum band both before and after correction for the contribution of measurement errors to the fluctuations. The latter quantities should be unbiased estimators of the nonlinearity parameter η. As Clavel et al. (1990) pointed out, there is a strong correlation between the degree of ionization and line variability in the sense that the lines generated by the most highly ionized species respond the most to continuum fluctuations.

Figures 9*a*–9*h* examine the same phenomenon in a different way. Here we plot the observed line flux $F_l(t + \tau_l)$ against the observed continuum flux $F_c(t)$, choosing τ_l as the lag at which the cross-correlation of that line with the 1300 Å band peaks. The dashed diagonal line passing through the origin and the mean of the observed line and continuum fluxes is the relationship that would be expected if the the line and continuum variations were perfectly correlated. Least-squares fits to the observed relations are shown as solid lines bracketed by dotted curves indicating the 1 σ uncertainty. In the language of the

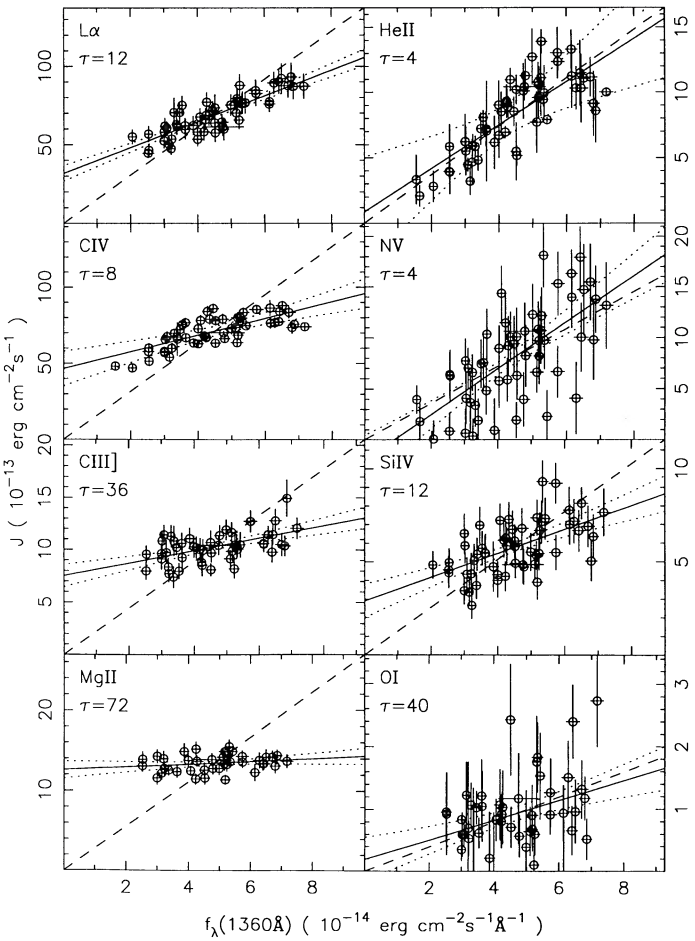

FIG. 9.—(*a–h*) Correlation of delayed line flux with continuum flux. The dashed diagonal line is the line of perfect correlation; the solid line is a least-squares fit, bracketed by dotted curves showing the 1 σ uncertainty.

TABLE 6

EMISSION LINE–CONTINUUM COVARIATIONS

Line (1)	$\frac{\delta F_l/\bar{F}_l}{\delta F_c/\bar{F}_c}$ Raw (2)	$\frac{\delta F_l/\bar{F}_l}{\delta F_c/\bar{F}_c}$ Corrected (3)	τ_l (days) (4)	$\frac{B_l}{\bar{F}_l}$ (%) (5)	$\frac{\bar{F}_l}{\bar{F}_c}$ (Å) (6)	$\frac{\partial(\ln F_l)}{\partial(\ln F_c)}$ (7)	$\eta_{\rm pred}$ (8)
N v λ1240	1.78	1.45	4	-28 ± 25	18 ± 1	1.29 ± 0.24	1.5
He II λ1640	1.10	0.91	4	9 ± 18	18 ± 2	0.91 ± 0.21	1.1
Lyα	0.58	0.51	12	49 ± 6	161 ± 3	0.51 ± 0.06	0.92
C IV λ1549	0.44	0.42	8	65 ± 6	158 ± 3	0.35 ± 0.06	1.1
Si IV λ1400	0.78	0.58	12	52 ± 12	13.2 ± 0.4	0.48 ± 0.11	0.70
C III] λ1909	0.47	0.35	36	73 ± 8	22.4 ± 0.5	0.27 ± 0.07	0.42
O I λ1304	1.97	0.32	40	26 ± 42	2.1 ± 0.4	0.74 ± 0.33	...
Mg II λ2800	0.23	0.12	72	93 ± 6	27.7 ± 0.4	0.07 ± 0.05	0.47

prologue to § 5, the slope of the best-fit line should be $\partial F_l/\partial F_c = \eta(\bar{F}_l/\bar{F}_c)$ in the limit that the line fluctuations follow the continuum fluctuations without smearing.

He II λ1640 and N V λ1240 appear to be linearly proportional to the continuum, but for Lyα, C IV, Si IV, C III] and especially Mg II, the linear extrapolation to zero continuum flux leaves a substantial fraction of the line emission unaccounted for. We may define the background line flux B_l as the intercept of the best-fit line with the vertical axis. This apparent background line flux has several possible interpretations: (1) It could be due in part to time delay smearing of the lines, which diminishes the fractional amplitude of their variations (we will test this explanation in the next subsection and find it is not a likely explanation). (2) It could imply an additive background source of line emission that is either not directly related to the observed continuum, or responds on a very long time scale. (3) It could be due to nonlinearity in the relation between line and continuum fluxes: nonlinearity would give a minimum background level $B_l = (1 - \eta)\,\bar{F}_l$. This last explanation is particularly plausible because in general we expect a nonlinear relation between line emissivity and continuum flux (see the discussion at the beginning of § 5).

The linear fits in Figures 9 are quantified in Table 6. Here for each line we give the adopted delay τ_l, the background line flux B_l as a percentage of the line flux F_l, the mean line flux divided by the mean continuum flux (i.e., the mean equivalent width of the line), and the measured η. The values in column (7) are in good agreement with those in column (3) except for the noisy O I line.

These observed values of η provide additional constraints on photoionization models. For example, in § 3.2 we constructed a two-zone photoionization model to reproduce the total line fluxes in NGC 5548. The η's predicted by that model are the final column in Table 6. The He II, N V, Si IV, and C III] lines match fairly well, but C IV and Lyα vary only one-third and one-half as much as the model predicts. Because the η predicted for Lyα by photoionization models is nearly always $\simeq 1$, independent of Ξ and p, and η predicted for C IV λ1549 is greater than 0.9 until Ξ gets to be so big that C becomes largely He- and H-like, this discrepancy is quite significant. Mg II λ2800 also appears to vary more weakly with changes in the continuum flux than the model predicts, but the predicted value of η for this line is much more sensitive to the free parameters.

A possible explanation for the discrepancy between the predicted and observed values of η for Lyα and C IV might be that the portion of the ionizing continuum most responsible for driving Lyα and C IV varies in step with the observed UV continuum, but with smaller amplitude. As Krolik & Kallman (1988) showed, it is the Lyman continuum which is most responsible for both these lines. Counting against this suggestion are the facts that the 1337 Å band is not far from the Lyman edge and that, over the range of wavelengths we observe, the amplitude of continuum variability seems to *increase* toward shorter wavelengths. However, if there is significant Lyman edge opacity in the continuum production region (as many accretion disk models predict), there may be countervailing tendencies.

5.3. *Deconvolution*

The data obtained by this experiment are the first to even approach the quality required to implement the Blandford & McKee (1982) program outlined at the beginning of this section. In fact, that paper concentrated on an even more ambitious goal—the geometrical structure as a function of line-of-sight velocity—which we shall not attempt here. However, even lowering our sights to obtaining the response functions for the total flux in the various lines leads to difficulties: because the power spectra drop so steeply toward higher frequencies, the Fourier transforms required are dominated by noise at the frequencies of interest.

To avoid this problem, we turn to a different deconvolution method, the method of maximum entropy. This method assumes that a process which we can model has rearranged the true "image" to produce the data we actually obtained. Although this rearrangement if often linear, linearity is not a prerequisite for use of the method. Trial solutions are fed through a model for the rearrangement and compared to the data. In order to select the "best" solution from among all those which, after passing through the model, fit the data to within a given criterion, an entropy function is defined for each image and the solution which maximizes this function is chosen. In other words, the image is adjusted until it gives a good fit to the data, and then any surplus structure in the image is ironed out by using the entropy criterion. Thus, to implement this method, we must first define an "image" space, then a model which rearranges the "image" into predicted observations, next choose a goodness-of-fit criterion, and finally define an entropy function.

The most important element of our "image" space is the set of response functions $\Psi_l(\tau)$ defined in the beginning of this section. However, this "image" space must be enlarged in several directions. First, the line fluxes near the beginning of the experiment depend on continuum fluctuations at unobserved times. We must therefore enlarge the "image" space to include the continuum flux at these earlier times. In fact, because the continuum flux even at measured times is only known to within some uncertainty level, the actual continuum fluxes at the observed times also lie in the "image" space. Finally, because of the presence of the background levels discussed in the previous subsection, we found we needed to generalize the relationship between line and continuum light curves given in equation (5.2). After experimenting with several alternatives, which gave similar results, we made the following choice:

$$F_c(t) = B_c(t) + \Delta F_c(t)\,,$$
$$F_l(t) = B_l(t) + \Delta F_l(t)\,,$$
$$\Delta F_l(t) = \int_0^\infty \Psi_l(\tau)\Delta F_c(t-\tau)d\tau\,. \qquad (5.5)$$

Here the continuum light curve $F_c(t)$ is expressed as the sum of two components, a nearly constant background $B_c(t)$ (which in practice we took to be exactly constant), and a more rapidly fluctuating component $\Delta F_c(t)$. The line light curves $F_l(t)$ are similarly decomposed into a nearly constant background $B_l(t)$, plus a fluctuating component $\Delta F_l(t)$. Thus, the "image" space is the union of the two functions $\Delta F_c(t)$ and $B_c(t)$ along with the 16 functions (two for each line) $B_l(t)$ and $\Psi_l(\tau)$. The rearrangement of the "image" space is the convolution which produces $\Delta F_l(t)$.

It is important to note that physical solutions for all the quantities in the "image" space must be positive, and the maximum entropy method automatically embodies this constraint. Other more direct linear reconstruction methods (e.g., Fourier inversion) do not possess this advantage.

The observations available to constrain the image are $F_i(t_i)$ and $F_c(t_i)$ at the times of observation t_i. The nearly equally spaced time sampling of the present data set is convenient for numerical evaluation of the convolution integral but is not an absolute restriction on the method. It does, however, have the signal advantage of substantially reducing the size of the image space because we would otherwise have gaps in the constraints on the continuum fluxes fed into the convolution. We define the quality of the fit by χ^2, and require $\chi^2/N = 1$, where N is the number of observations.

We define the entropy per image pixel as $p - q - p\ln(p/q)$, where p is the image value and q is the corresponding default value. Differentiation of this function with respect to p shows that entropy is maximized when $p = q$. In this application, we must of course assign an appropriate default value to each of the subimages rather than using the same default level over the whole image. Normally the default image $q(t)$ is a uniform image equal to the average value of $p(t)$, and the maximum entropy fit can be thought of as the most *uniform* positive image that is consistent with the observations. Here we sometimes found it useful to also employ the so-called *curvature* default, $q(t) = [p(t - \Delta t)p(t + \Delta t)]^{1/2}$. When curvature defaults are used, the entropy becomes a measure of the local curvature, and the maximum entropy fit gives, roughly speaking, the *smoothest* positive image that fits the data. This choice embodies a physical assumption that the line emissivity varies smoothly across isodelay surfaces.

The numerical algorithm we used to find the maximum entropy fit is a variant of the general algorithm described by Skilling & Bryan (1984), as implemented in the software package MEMSYS. This algorithm performs iterative corrections to an image p in order to maximize the functional $Q = \Gamma S(p) - \chi^2(p, D)$, where $S(p)$ is the entropy of the image, χ^2 is the data constraint statistic, which is a function of p and the data D, and the positive scalar Γ is a Lagrange multiplier used to control the relative importance of the entropy and data. Because the full dimension of the image space is often impractically large, the problem is solved repeatedly in a series of subspaces spanned by a small number of image vectors, including p, $p\nabla S$, and $p\nabla\chi^2$, which are evaluated anew on each iteration. Each iteration uses local quadratic approximations for S and χ^2 to move within the subspace toward a maximum of Q for some value of Γ. The starting point is a uniform image, which is the solution for $\Gamma = \infty$, i.e., completely ignoring the data. In the early iterations the value of γ is lowered a bit each time to gradually bring on the data constraint until the desired χ^2 is reached. In the final iterations Γ is set to maintain the desired χ^2 while further increasing the entropy. Convergence is confirmed via a small value of the statistic

$$\text{TEST} = \frac{1}{2}\left|\frac{\nabla s}{|\nabla s|} - \frac{\nabla\chi^2}{|\nabla\chi^2|}\right|^2, \qquad (5.6)$$

which measures the degree of nonparellelism between the gradients of S and χ^2. Linear problems generally converge in ~ 30 iterations, but we require several hundred iterations to reach TEST $\sim 10^{-4}$, because our problem is nonlinear and we recalculate the default image between iterations.

Figures 10 and 11 show two examples of the fitted line and continuum light curves and the corresponding reconstructed response functions obtained by the maximum entropy method. At the bottom of these figures, the continuum light curve (*solid curve*) is tightly constrained by the observations (vertical error bars). Above the continuum panel we show for each line the

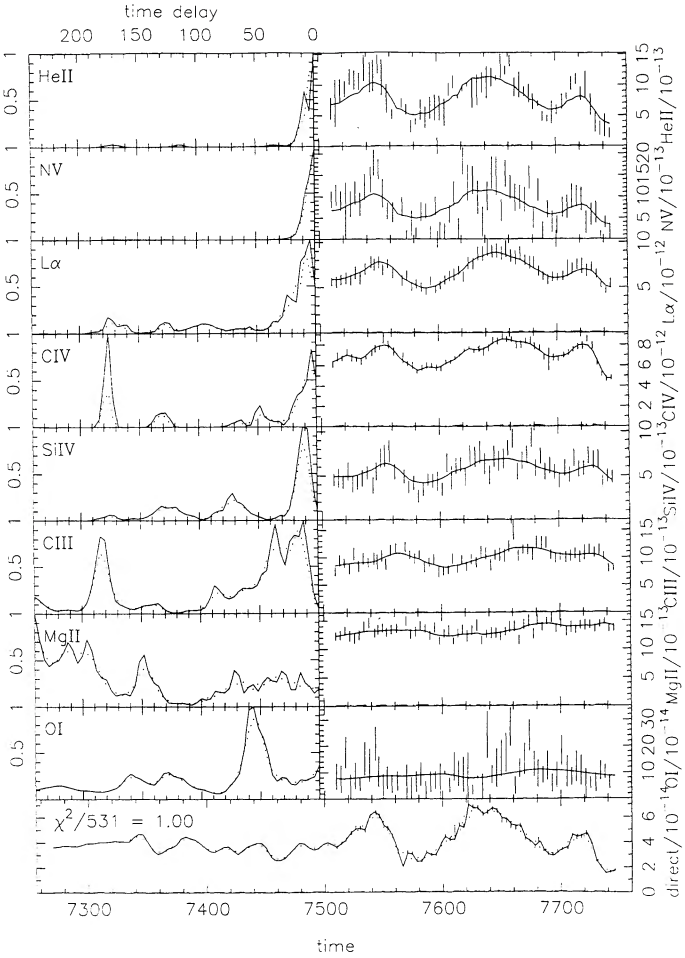

FIG. 10.—Maximum entropy reconstruction of the response functions for zero background default.

reconstructed response function on the left, and the predicted light curve fitted through the observed line fluxes on the right. We have arranged the lines in order that the width of the main peak of the response function increases progressively from top to bottom. The background light curves for the continuum and for each line are indicated by dashed curves. The default levels are shown as dotted curves. We have generally used curvature defaults for the continuum light curve and the line response functions, and uniform defaults for the background light curves.

The model is powerful enough (has enough degrees of freedom) to fit to the data very well—an arbitrarily small value of χ^2 can be achieved. For the reconstructions we present the reduced χ^2 over the entire data set is unity. The fitted light curves tend to have less extreme maxima and minima than would seem to be justified on the basis of the observations. This is typical of maximum entropy fits constrained by the χ^2 statistic, and is a consequence of the entropy trying to minimize the image structure against the pull of the data.

The reconstructed response functions for most of the lines have a robust main peak near zero delay. However, there are a range of solutions, all fitting the data with $\chi^2/N = 1$, which differ in detail depending on the choice of line and continuum background levels, uniform versus curvature defaults, and the maximum time delay in the response function. In order to

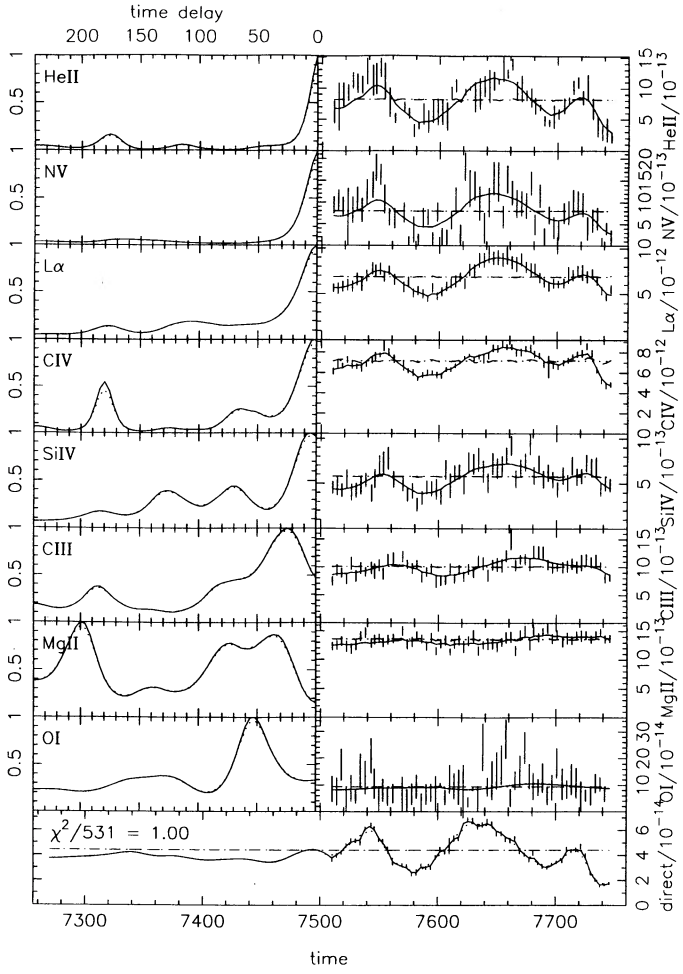

FIG. 11.—Maximum entropy reconstruction of the response functions for background defaults equal to the mean fluxes.

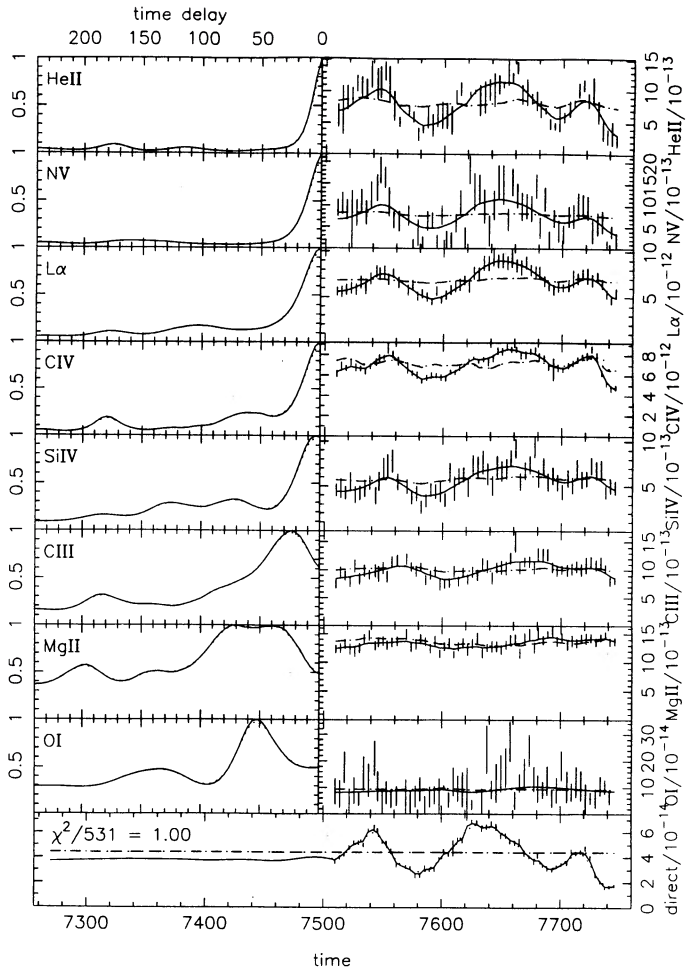

FIG. 12.—Maximum entropy reconstruction of the response functions for curvature defaults for the line background fluxes.

understand which aspects of the solution are robust and which may be artifacts of the particular reconstruction method, we consider the examples shown in Figures 10–13.

Figure 10 shows the results of a fit for the case in which the line and continuum backgrounds are given very small default levels, effectively eliminating those degrees of freedom from the model. This model tests the hypothesis that the line fluxes vary in linear proportion to the delayed continuum, which is probably a poor assumption given the results presented in § 5.3. A formally acceptable fit to the data has been found, but the solution is hard pressed to do so as indicated by the jagged structure in the response functions. The poor results obtained with this model give us confidence that the background fluxes noted in Figure 9 are not due to time-smearing of the lines.

In Figure 11 the background default levels are set equal to the mean of the observed continuum and line fluxes. Now the backgrounds account for the mean line and continuum fluxes, and the response functions account for the fluctuating components. For all lines the general structure of the response functions in Figure 11 are quite similar to those in Figure 10, but the response functions are now much smoother. Nonlinearity of response is a possible explanation for the improved results. In the limit of low-frequency fluctuations $F_l = \bar{F}_l(1 + \eta\,\delta F_c/\bar{F}_c)$, so that when $F_c = 0$, $F_l = (1 - \eta)\bar{F}_l$. Thus, for any $\eta < 1$, a positive background level is required, but it need not be greater than $\bar{F}_l$ as long as $\eta > 0$. As Table 6 shows, all the empirical estimates of η (save for N v λ1240) lie between 0 and 1. When $\eta > 1$, the *minimum* background level is negative, but larger values can still give consistent solutions. Thus, $\eta < 1$ for many of the lines may explain why the zero background level solutions are less satisfactory.

In Figure 12 we give the line backgrounds even more flexibility by switching from uniform to curvature defaults. The background is now used to fit certain details of the line light curves, and this allows various bumps in the tails of the response function to relax relative to the main peak. In Figure 13 we chop off the tail of the response functions at 60 days rather than 240 days.

The features in the response functions at time delays between 50 and 200 days have uncertain reliability. We cannot rule out that they are true features; indeed, one possible model for the site of C III] λ1909 production requires them (see § 6.3). However, there are also indications that they are artifacts of the relatively small number of data points constraining the response functions at such long lags. We have run a number of tests with simulated datasets which lead us to suspect that these bumps may be unreliable.

In one test we constructed a continuum light curve using a

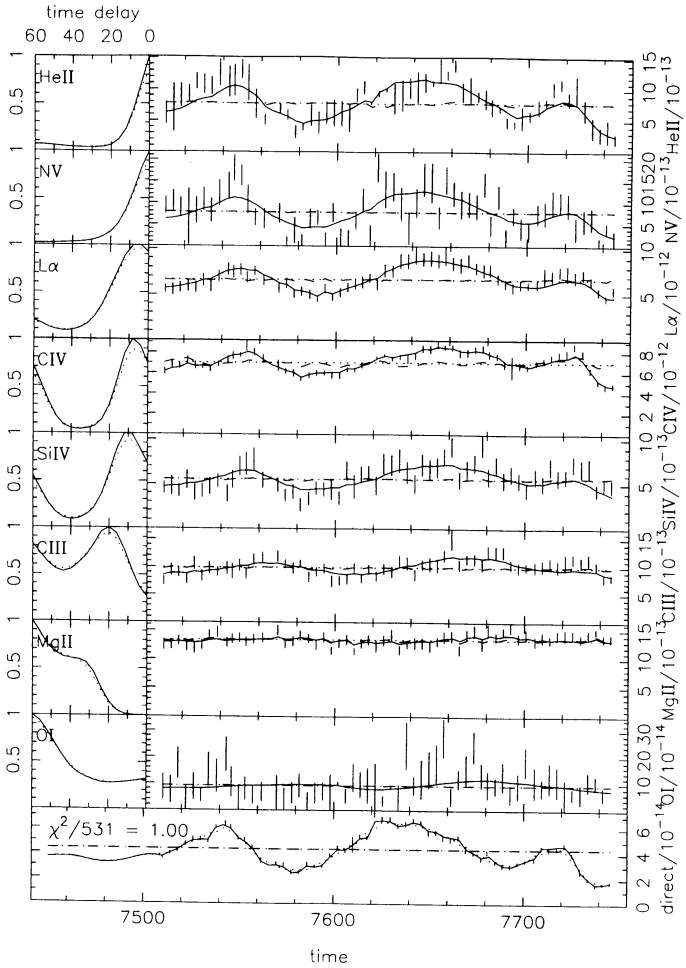

FIG. 13.—Maximum entropy reconstruction of the response functions for background defaults equal to the mean fluxes, but only permitting the response functions to extend to 60 days.

pure sinusoid with a period of 100 days, and a line light curve which was identical to the continuum light curve except that it was delayed by 20 days. Noise was then added using the same time sampling and statistical error bars as in the real data. The response function reconstructed from the simulated data had a large peak at 20 days, and a smaller peak at 120 days, yet the true response function was a delta function at 20 days. This example illustrates how the presence of a strong periodic signal in the continuum light curve can give rise to sidelobes in the response function. These sidelobes have a very direct physical interpretation: to the extent that the continuum is periodic, earlier features look identical to the most recent ones, and there is a fundamental ambiguity in identifying which one is responsible for a given structure in a line light curve.

The bumps near delays of 180 days found in the response functions for He II λ1640, Lyα, C IV λ1549, and C III] λ1909 may all represent examples of this ambiguity. The continuum light curve exhibits a strong quasi-periodicity with a period of ≃90–days, so peaks near 180 days could well be due to an artificial "look-back" of two continuum quasi-periods. On the other hand, the absence of bumps at 90–100 days argues against this interpretation. Until more data constrains the long lag behavior of the response functions, we are reluctant to ascribe much significance to these features.

The main peak near zero time delay in most of the lines is the most robust aspect of the reconstructed response function. The width and centroid of the primary response peak differ significantly from line to line, presumably reflecting the ionization structure of the emission-line regions. He II and N V have the narrowest response functions, sharply peaked at zero time delay and dropping to half-maximum within 10 days. The response functions of Lyα and C IV are slightly broader, 12–15 days at the half-maximum point, and sometimes but not always peaking at 5–7 days rather than at zero delay. The Si IV response peaks at 5–10 days and drops to half-maximum around 20 days. The C III] response peaks at 20–30 days and is 40–50 days wide at half-maximum, or less if there is a significant background. Mg II may have a peak around 30–40 days, but its response function is generally very wide in order to wash out continuum variations. Finally, the O I observations are so noisy that very little structure develops in the light curve, and the structure in the response function is not reliable for this line. One must also bear in mind that these are the smoothest positive response functions that fit the data. The true response functions may have sharper features.

6. GEOMETRY OF THE BROAD-LINE REGION

6.1. *Building Blocks*

As we discussed at the beginning of § 5, the meaning of the response functions is that they represent the marginal increase of line luminosity due to a change in the continuum luminosity, integrated over individual surfaces of constant delay. Because we know the ionizing luminosity, if we knew the geometrical distribution of emitting material and the pressure as a function of location, we could then predict the response function appropriate to relating observed continuum fluctuations to observed line fluctuations:

$$\Psi_l(\tau) = \int d^3r n_{\rm cl}(\boldsymbol{r}) \frac{A_{\rm cl}(\boldsymbol{r})}{4\pi r^2} \frac{F_{\rm ion}}{F_c} \frac{\partial}{\partial F_{\rm ion}} \times \{S_l[F_{\rm ion}, p(\boldsymbol{r}); \theta]\} \delta\left[\tau - \frac{r}{c}(1 - \cos\theta)\right], \quad (6.1)$$

where the local density of emitting clumps is $n_{\rm cl}$, and the mean emitting surface area of each clump is $A_{\rm cl}$; S_l is the flux in line l from each clump radiated toward the observer, for θ defined as the angle between the line of sight and the line connecting the continuum source with the position of the emitting material; the continuum is assumed to be radiated isotropically, and to rise and fall with no change in spectral shape so that the ratio between the observed continuum flux and the ionizing continuum flux remains constant at $F_c/F_{\rm ion}$; and p is the gas pressure. The δ function picks out the surface of delay τ. We assume that there is no obscuration anywhere in the system. In the continuum limit (i.e., $\int d^3r n_{\rm cl} \to \infty$ while $\int d^3r n_{\rm cl} A_{\rm cl}$ remains finite), this form can describe smooth distributions, for example, disk surfaces.

If the physical quantities are distributed with spherical symmetry about the continuum source, equation (6.1) may be simplified to a single integral:

$$\Psi_l(\tau) = \frac{c}{2} \int_{c\tau/2}^{\infty} dr \frac{n_{\rm cl}(r) A_{\rm cl}(r)}{r} \frac{F_{\rm ion}}{F_c} \frac{\partial}{\partial F_{\rm ion}} \{S_l[F_{\rm ion}, p(r); \mu(r, \tau)]\}, \quad (6.2)$$

where $\mu(r, \tau) = 1 - c\tau/r$ and the lower limit on the integral comes from the fact that the greatest lag from a given radius is $2r/c$, achieved when the material is exactly on the opposite side from the observer. If the emitting material is in a spherical shell at radius r and emits isotropically, $\Psi_l(\tau)$ is simply a square wave extending from $\tau = 0$ to $\tau = 2r/c$ whose amplitude is proportional to the fraction of the change in continuum flux going into that line.

Similarly, if the emitting material radiates isotropically but is confined to a thin annulus of radius r tilted to the line of sight by an angle i, $\Psi_l(\tau) \propto \{[\sin^2 i - (c\tau/r - 1)^2]^{1/2}\}^{-1}$. In this case, Ψ_l is a double-horned curve diverging at the end points $(1 \pm \sin i)r/c$. In the limit of $\sin i = 0$, Ψ_l for a ring becomes $\propto \delta(\tau - r/c)$. The response function takes on a different shape if the material radiates anisotropically, even if it is distributed spherically. If, for example, it radiates $\propto 1 - \cos\theta$ (like the phases of the Moon), $\Psi_l(\tau)$ rises linearly from $\tau = 0$ to $\tau = 2r/c$, where it plunges down to zero again. More general distributions with either spherical or disklike symmetry can be built up by superposition of these basis functions with varying values of the scale and varying amplitudes.

Because the shape of the response function depends both on the angular radiation pattern of the line and on the geometry of emitting material, we must use our knowledge of line radiation transfer to separate out the two effects. Two of the lines—C III] λ1909 and He II λ1640—are almost guaranteed to be emitted isotropically because the material is almost surely transparent to them. C III] λ1909 is an intercombination line, so its oscillator strength is very small. He II λ1640 is a recombination line (the He II analog of Hα) whose lower state is so much higher in energy than the ground state that it never collects significant population.

In the case of two other lines—N V λ1240 and Si IV λ1400—the optical depth is likely to be large, but is probably not as large as the thermalization depth, i.e., the optical depth such that the collisional de-excitation rate matches the spontaneous emission rate times the escape probability (as shown by photoionization models like the ones discussed in § 3.3). For such lines, the angular radiation pattern depends primarily on the shape of the emitting clumps. If their transverse dimensions were comparable to the thickness of the zone emitting these lines, the lines would be radiated more or less isotropically. However, if the line-emitting clumps are optically thick in the Lyman continuum, the zone emitting these lines is a relatively thin layer on the illuminated edge of a considerably thicker structure, so that the lines' angular radiation pattern is the product of the structure's projected size on the sky and a limb-darkening law very similar to that of electron scattering in a plane-parallel atmosphere. If there is no optically thick structure behind the line-emitting zone (e.g., a star or an accretion disk), both faces of the layer are equally bright because continuous opacity for these lines is small (the Balmer continuum edge is the only contributor). C IV λ1549 is almost in this category, but its optical depth can, in some cases, be large enough to begin thermalization. When that happens, its angular radiation pattern favors the illuminated side.

Finally, Lyα can present the most extreme case of expected anisotropy. If the Lyman edge optical depth is $\lesssim O(10)$, its angular radiation pattern will be similar to the resonance lines. However, if low ionization lines like Mg II λ2800 are produced from the same material, and if collisional enhancement of the Balmer lines is required to match the observed line ratios (as is often the case), the Lyman edge optical depth must be much greater than this, and Lyα will be thermalized. In that case, the illuminated side is very strongly favored: its surface brightness in Lyα can be easily two or three orders of magnitude greater than the shadowed side's (Kwan & Krolik 1981).

6.2. *Construction*

To arrive at a geometric model for the line-emitting region, we must combine the basis functions of § 6.1 with the empirically derived response functions found in § 5.2, following the guidelines of § 6.1. The method we choose is to follow the grouping into high- and low-ionization lines discovered in the response functions (§ 5.2). Within each group, we focus attention on those lines for which we have reason to believe the emission is isotropic, in order to eliminate the complications of possible dependence on θ in S_l.

First consider Lyα, C IV λ1549, He II λ1640, N V λ1240, and Si IV λ1400. The shapes of the response functions for these five lines are all quite similar: roughly speaking, they decline monotonically from peaks at or near zero lag to low levels which extend from 20^d out to 50^d or more. We have already argued that He II λ1640 should always be emitted isotropically, but that the angular radiation pattern for the others depends on the shape of the emitting clumps. Because all the rest of these lines have response functions very similar to that of He II λ1640, we make the *Ansatz* that they are all emitted (roughly) isotropically. This will be true for C IV λ1549, N V λ1240, and Si IV λ1400 if the emitting clumps are not too elongated or sheetlike; it will be true for Lyα if, in addition, the clumps have Lyman edge optical depths $\lesssim O(10)$. Our last supposition is that the emitting region is roughly spherical. Our argument is based on the large apparent covering fraction of line-emitting material: the estimated covering fraction of the high-ionization zone in the two zone model (§ 3.3) is $\simeq 0.3$; at a bare minimum it must be at least 0.16, the ratio of the summed flux of the five high-ionization lines to the ionizing flux. Unless the spectrum has a very large bump in the EUV, this material must cover a significant part of the solid angle around the continuum source. In principle, it would be possible to construct a model in which the line-emitting region is a sequence of nested thick disks, but we follow the spherical model first as it involves fewer free parameters.

Given the assumptions of isotropic radiation and spherical symmetry, there is a simple relation between the distribution in radius of the emitting material and the functions $\Psi_l(\tau)$. To describe it, we first define the covering factor

$$C(r) = \int_0^r dr' \, \tfrac{1}{2} n_{\rm cl}(r') A_{\rm cl}(r') \, , \tag{6.3}$$

where the factor of $\frac{1}{2}$ is appropriate for slab clumps. After rewriting the integrand of equation (6.2) in terms of the covering factor, a differentiation yields

$$\frac{dC(c\tau/2)}{dr} = -\frac{\tau}{c} \frac{F_c}{F_{\rm ion}} \frac{d\Psi_l/d\tau}{\partial S_l/\partial F_{\rm ion}} \, . \tag{6.4}$$

The rate of increase of the covering factor at any given radius can then be found by searching through a grid of photoionization models for the physical conditions such that the right-hand side of equation (6.4) is most nearly the same for all the different lines.

To do this in a quantitative way we defined a second figure of merit $\Phi_2 = \sum_j \phi_{2j}$ where the sum is over the various lines,

TABLE 7

THE RADIAL RUN OF PHYSICAL CONDITIONS IN THE BROAD EMISSION-LINE REGION

Lag	Ξ	p (dyne cm^{-2})	Φ_2	$r_{\rm pred}$ (lt-day h^{-1})	$C(\leq r)$
4^d	0.56	0.027	1.1	32	0.00080
8	0.56	0.027	0.73	32	0.0026
12	0.42	0.27	0.59	12	0.12
16	0.24	0.27	0.48	15	0.26
20	0.24	0.27	0.37	15	0.41
24	0.10	0.27	0.42	24	0.50
28	0.10	0.27	0.85	24	0.62
32	0.10	0.27	1.09	24	0.67

NOTE.—If the isotropic radiation, spherical symmetry model is correct $r_{\rm pred}$ should be $c\tau/2$ (eq. [6.4]).

and ϕ_{2j} is given by

$$\phi_{2j} = \left(\frac{Q_j^2}{\bar{Q}^2} - 1\right)^2 ,$$

where $\bar{Q}^2 = (1/N)\sum_j Q_j^2$, N is the number of lines in question, and Q_j is the ratio of the marginal line emissivities to the response function derivative for the line in question. We then assumed the hardest plausible accretion disk fit (§ 3.1) for the ionizing spectrum.

Finally, using the relation between ionization parameter and local continuum flux $\Xi = F_{\rm ion}/(cp)$, we solved for $r_{\rm pred}$, the size predicted for the emitting region by these photoionization models.

Results of this procedure applied to Lyα, C IV λ1549, He II λ1640, N V λ1240, and Si IV λ1400 are shown in Table 7. As can be seen, reasonable (i.e., $\Phi_2 < 1$) photoionization fits can be obtained at each lag from 8^d to 28^d (corresponding to radial distances from 4 lt-day to 14 lt-day). For each of these, we define a predicted scale by solving the relation $\Xi = L_{\rm ion}/(4\pi r^2 cp)$:

$$r_{\rm pred} = 3.9 p^{-1/2}\Xi^{-1/2}h^{-1}\text{lt-day} . \quad (6.5)$$

We find that for $12^d \leq \tau \leq 24^d$ $r_{\rm pred} \propto \tau$ as it should. More precisely, $r_{\rm pred}$ agrees with the actual scale to within a factor of 2–4 (depending on choice of Hubble constant). A factor of 3 in the predicted distance corresponds to a factor of 9 uncertainty in the product $p\Xi$, which is certainly well within the uncertainty of the fit, for the values of $\partial S_l/\partial F_c$ change relatively slowly over the grid. It is also highly encouraging that the parameters of the high ionization zone of the best-fit two-zone model (§ 3.3) are squarely in the middle of the range of these parameters, inferred by an entirely independent argument.

The relatively poor fit at small lags is probably a symptom of the flattening near zero lag in the response functions for Lyα, C IV, and Si IV (see Figs. 11, 12, and particularly 13). The most plausible interpretation of this flattening is that it marks the radius of the innermost shell contributing to the line emission. Because this flattening occurs around 4–8^d lag, and the sampling interval was only 4^d, it is hard to be too precise, but this interpretation suggests there is little line-emitting material inside ~4 lt-day.

The pressure in this portion of the broad-line region is nearly constant at a value $n_{\rm H} T \simeq 2 \times 10^{15}$ K cm^{-3}. The temperature at the illuminated edges of these clouds varies from $\simeq 2 \times 10^4$ K at a radius of 12 lt-day to $\simeq 4 \times 10^4$ K at $r = 4$ lt-day, so the associated H nucleus density stays almost constant at $\simeq 5$–10×10^{10} cm^{-3}. If the emitting material has a column density of no more than 10^{22} cm^{-2}, the maximum Lyman edge optical depth in any of this material inside $\simeq 10$ lt-day is $\simeq 2$, so Lyα should indeed have the same angular radiation pattern as the other resonance lines.

Table 7 also shows the cumulative covering factor, integrated from the center outward. Another test of the quality of the photoionization models is provided by the match between the covering factor for high-ionization lines found from consideration of mean line fluxes (0.3) and the covering factor found from this model based on fluctuations (0.5–0.7, depending on where one sets the somewhat imprecisely determined outer bound of this region). Although significant material can be found close in, dC/dr actually peaks between 8 and 10 lt-day (lags of 16^d–20^d). It is also important to note that the integrated mass in line-emitting material is

$$M(r) = \int_0^r dr' 4\pi r'^2 \frac{dC}{dr'} N(r')\mu_{\rm H} , \quad (6.6)$$

where $\mu_{\rm H}$ is the mass per H atom so that the mass in line-emitting material is predominantly found at the larger radii.

The high and nearly constant pressure in this inner region places strong constraints on any gas in pressure equilibrium with the line-emitting material. To avoid pressure gradients due to the gravity of the central black hole, the temperature of this gas must be at least $\simeq 7.5 \times 10^9 (M/2 \times 10^8\ M_\odot)(r/10$ lt-day$)^{-1}$ K. Given the assumption of pressure equilibrium, its density is then less than $\simeq 1 \times 10^5 (M/2 \times 10^8\ M_\odot)^{-1}(r/10$ lt-day$)$ cm^{-3}.

Consider the low-ionization lines next. Of these (C III] λ1909, Mg II λ2800, and O I λ1304), only C III] λ1909 has a reasonably well-defined response function, and only C III] λ1909 can be expected to be radiated isotropically. We therefore concentrate on it alone. Its response function (Fig. 11) has a clear peak at 20^d–30^d. No spherically symmetric distribution can produce this shape because any sum of square waves all beginning at zero must have its peak at zero. An exactly edge-on disk is similarly ruled out. On the other hand, oblique flattened distributions characteristically have a double peak and a central minimum. In the simplest model of this sort, the line luminosity from successive rings of constant width and increasing radius would increase from small radius up to a maximum at radii between 20 and 30 lt-day, and then decrease outward.

However, this model is very difficult to understand in terms of photoionization physics. Modulo our uncertainty about the shape of the ionizing spectrum and the value of the Hubble constant, we know the ionizing flux at 25 lt-day from the center. The only remaining free parameter is the pressure. However, if the pressure is low enough for C III] λ1909 to avoid collisional de-excitation (i.e., $n_{\rm H} \lesssim 10^{10}$ cm^{-3}), Ξ is then so large that very little C III is present in the ionization balance. On the other hand, if the pressure is high enough to allow substantial abundance of C III, it is too high to allow significant radiation in the λ1909 line.

Only two geometrical solutions appear to be consistent with all the data. In one, the low-ionization region lies at a distance ~100 lt-day from the source of the ionizing flux, but the angle between its position and the line of sight is comparatively small, $\simeq 45°$. The delay, $\tau = (r/c)(1 - \cos\theta)$ is then reduced to

$\simeq 25^d$. This material cannot lie directly on the line of sight because we see no evidence for soft X-ray absorption. On the other hand, its estimated covering fraction ($\simeq 5\%$: § 3.3) is small enough that θ for this gas could well be small, yet still nonzero. The fact that C III] exhibits by far the biggest velocity offset from systemic of any of the UV lines (1200 km s^{-1} of blueshift) also hints that there may be something special about the geometry of its source. Nonetheless, this model does appear highly contrived.

In the second model, we suppose that the low-ionization material occupies a somewhat thickened annulus whose radius is $\simeq 100$ lt-day, and whose normal has an inclination angle relative to the line of sight such that $\sin i \simeq 0.75$. Now the peak in the response function is the inner horn of the two-peaked ring response function, while the outer horn is the feature at $\simeq 180^d$ (see Figs. 10–12). As was discussed in § 5, the reliability of this feature is open to doubt because the monitoring data contains relatively few pairs of line and continuum fluxes separated by such a large amount. Balmer line data from the complementary ground-based program (Peterson et al. 1990) will be very important in clarifying this point, though it will be harder to interpret because of the likely asymmetry in Balmer line emission from optically thick clouds and because the Balmer lines are sensitive to the strength of the soft X-ray continuum which may vary quite independently from the UV continuum. This last point (sensitivity to independent fluctuations in the soft X-ray band) may also explain the lack of response of Mg II $\lambda 2800$ to the observed UV continuum fluctuations.

Note that there is no evidence for low-ionization species in the innermost part (i.e., $r \leq 12$ lt-day) of the emission-line region. C III] $\lambda 1909$ appears to come from a larger zone, while to the extent that any information can be drawn from them, the response functions for O I $\lambda 1304$ and Mg II $\lambda 2800$ both peak at much larger delays. Therefore, the traditional arguments for optically thick clouds (e.g., Kwan & Krolik 1979, 1981; Weisheit, Shields, & Tarter 1981) do not necessarily apply inside $\simeq 10$ lt-day in this Galaxy.

This picture of two separate structures, a roughly spherical high-ionization zone and a flattened low-ionization zone, is similar to the picture advocated by Collin-Souffrin and collaborators (as reviewed in Collin-Souffrin & Lasota 1988), but with a significant difference. In this picture, C III] $\lambda 1909$ is emitted from the flattened low-ionization zone, while in theirs the density in the low-ionization zone is far too high to permit significant emission in that semiforbidden line.

Our final comment on the geometry of the low-ionization material is to point out that if our line of sight does lie near its plane (our second attempt to reconcile photoionization models and the C III] response function), that this plane is inclined substantially with respect to the plane of the outer Galaxy, which is nearly normal to our line of sight.

6.3. *Dynamics*

Based on comparisons of high signal-to-noise line profiles and plausible arguments about the physical conditions in broad line clouds, Shuder (1982) argued that lines with higher velocity widths should be produced closer to the ionizing source. Although the *IUE* spectra do not permit detailed profile analysis, we can test Shuder's hypothesis by correlating the velocity widths of the emission lines with the locations of their production. A simple way of performing this comparison is to plot the width σ of the single Gaussian fit to each line against the position τ_l of the peak in its cross-correlation with the 1337 Å continuum. As Figure 4 shows, there is a definite correlation. The best fit to the points in Figure 4 gives $\sigma \propto \tau_l^{-0.51}$, with an uncertainty in the exponent of approximately ± 0.2.

One possible source for the velocity of the line-emitting material is the gravitational potential of the central black hole. To order of magnitude, velocities should scale as $(GM/r)^{1/2}$, but different pictures (e.g., circular orbits, random motions, radial free-fall) prescribe different coefficients of order unity. The curve in Figure 4 is a least-squares fit to the form $\sigma = (GM/r)^{1/2}$ whose value of $M = 2.7 \times 10^7\ M_\odot$. If the motions were circular orbits, this would be the implied central mass; if they were randomly directed orbits, the implied mass would be three times greater. In order to agree with the mass obtained from the accretion disk fit to the UV continuum ($1 \times 10^8\ h^{-1}/\sin i\ M_\odot$), the orbits would have to be partially confined to a plane roughly perpendicular to the line of sight. However, the accretion disk fit—and the radius estimate provided by τ_l—are sufficiently uncertain that such specific claims are completely unwarranted. All that can really be said is that the distribution of line widths with delay is consistent with gravitational dynamics being the source of the motion, and a central mass $\sim 10^7$–$10^8\ M_\odot$.

In principle, a superior way of doing this analysis would be to use the distribution in emission we have already found, as defined by dC/dr and the line emissivities calculable by photoionization models. Unfortunately, much of the strength of the correlation shown in Figure 4 is due to the low-ionization lines, for which the response function deconvolution did not produce an unambiguous radial distribution. In the long run, the most productive way to use the profile data will be to examine profile variability in the spirit of Blandford & McKee (1982).

7. SUMMARY

In this paper we remarked that AGN variability studies have twin goals: to illuminate the mechanisms responsible for continuum production and to map out the photoionized emission-line region. The results of the NGC 5548 monitoring experiment have permitted substantial progress on both fronts.

Using this data set, we have now severely constrained the nature of fluctuations in the inner portion of the accretion disk in this active galactic nucleus. Because the power spectrum of continuum fluctuations is dominated by time scales of ~ 100 times the orbital period at the place where the photons are generated, local orbital dynamics cannot explain these fluctuations. At least two other mechanisms are possible: orbital dynamics much farther from the central black hole may create perturbations which propagate inward; or the perturbations may be created locally by radiative cooling dynamics if the surface density of the accretion disk (i.e., its thermal inertia) is great enough.

Over the range of frequencies where we have measured the continuum power spectrum [$(240^d)^{-1}$–$(30^d)^{-1}$], it is roughly a power law with index between -2 and -3. It is possible that the power-law shape of the power spectrum can be explained by the power-law dependence of most dynamical variables on radius, and the spread in radii contributing to individual continuum bands. In a model-dependent way (i.e., by assuming how the local fluctuation frequency scales with radius), one may use the logarithmic slope of the power spectrum to estimate the way the amplitude of fluctuations scales with radius.

For example, if the local frequency is $\propto r^{-3/2}$ as would be predicted by either orbital dynamics or optically thick cooling, $\delta T/T \propto r^{-\beta}$ with $-0.15 \lesssim \beta \lesssim 0.6$.

Fluctuations at all continuum bands from 5000 Å to 1300 Å are very well correlated with lags of no more than $\sim 2^d$, although their fractional amplitude does systematically decline toward lower photon frequencies. At the very least, the centroids of the regions responsible for the different bands must lie within 2 lt-day of each other. Within the context of specific continuum production models, e.g., accretion disk models, stronger statements may be made. Most notably, if the continuum is radiated by a thermal accretion disk, the disturbances responsible for the continuum fluctuations must have a radial group velocity greater than $\sim 0.1c$. It is possible that this high group velocity is due to the fluctuations at longer wavelengths being driven by reprocessing of photons initially of higher energy.

Some of the decline in fractional amplitude of variation toward longer wavelengths is due to increasing dilution with starlight or other sources of radiation (e.g., Balmer continuum, merged Fe II emission lines), but some of it appears to be intrinsic to the accretion disk. To the extent that our simple accretion disk model for the fluctuations is accurate, we can estimate the degree by which the local emission deviates from a blackbody. Parameterizing this deviation by a multiplicative factor of $(h\nu/kT)^q$, we find that $q \simeq -0.2$.

This excellent data set also permits, for the first time, true multizone modeling of the broad emission-line region, as well as a direct determination of the distance scale within that region. Using the deconvolution formalism of Blandford & McKee (1982) (although we employ the maximum entropy method to actually solve the convolution equation), we have found the response functions for each of the eight emission lines measured. The high-ionization lines all have peak response near zero lag, and decline to a low pedestal by 15–20 days lag. Because it exhibited by far the most significant variations of the low-ionization group, only C III] λ1909 yielded a well-defined response function, but it is quite distinct in character from the high-ionization group. It has a distinct low point at small lags, peaks near 25 days lag, and rolls off slowly toward longer lags. When the response functions are studied out to large lags (>60 days), sometimes features are found in the neighborhood of 180 days, but their reliability is suspect.

Arguing on the basis of the large covering factor required to explain the strength of the high-ionization lines ($\simeq 30\%$), we modeled the geometry of the high-ionization zone as a spherically symmetric system with locally isotropic line radiation. The quality of the latter assumption depends on the shapes of the emitting regions. With these assumptions, the response functions can be converted to a map of line-emitting covering fraction with radius via photoionization modeling. We found that at each of the lags in the range 8–28 days (corresponding to radii from 4–14 lt-day) decent fits could be found and that the derived pressure was nearly constant with radius at $\simeq 2 \times 10^{15}$ K cm^{-3}. The derived ionization parameter Ξ falls with increasing lag according to an inferred distance scale which checks with the time delay to within a factor of $2h^{-1}$. Given the uncertainties of the modeling procedure, this level of agreement is truly remarkable: it corresponds to a factor of $4h^{-2}$ error in the product of $p\Xi$. The column density of clouds in this portion of the broad line region is probably $\sim 10^{22}$ cm^{-2}, a number fixed primarily by the requirement of permitting isotropic radiation of Lyα. The usual arguments for optically thick clouds in the broad-line region do not apply to these because there is no evidence for strong Mg II λ2800 or Balmer line emission from this zone.

The low-ionization lines are probably made at larger distances, but the circumstances in this region are less well determined by the NGC 5548 data. Distances of at least 25 lt-day are clearly required, as is at least some flattening of the material's distribution. However, it is possible that the true characteristic scale is as large as ~ 100 lt-day. When it becomes available, the results of the complementary ground-based monitoring will be vital for refining our picture of the low-ionization region.

The last remaining questions are how well these results generalize to other active galactic nuclei, and to what degree models based on mean line ratios have been confirmed or denied. In the past, the physical conditions in the broad emission-line region were generally inferred from a grab bag set of mean line ratios as modelers attempted to produce a description that both averaged over different zones within single objects and over the entire ensemble of objects. Our study of NGC 5548 is one of the few concentrating on a single object, and so we do not know whether our inferred conditions can be taken as representative. It may be significant in this regard that, in contrast to the efforts based on fitting a collection of different sources, we found that a two-zone photoionization model was required even to fit the mean line ratios. With respect to the validity of mean flux photoionization models, our results provide a split decision: the fluctuation analysis confirms part of the model specific to NGC 5548 (the character of the high-ionization, high-pressure region), while only weakly constraining the second (low-ionization, low-pressure) zone; on the other hand, in at least this one case, it is clear that there is substantial line emission coming from a region whose pressure is ~ 30 times higher than had previously been thought, on the basis of single zone photoionization models, to be typical of the broad emission-line region.

J. H. K. was partially supported by NASA grants NAGW-1017, NAGW-1194, and NAGW-2012. He also thanks Jim Pringle for helpful conversations about accretion disk dynamics. All the authors thank the replacement referee, Simon Morris, for his thorough—and rapid—review of the paper.

REFERENCES

Bahcall, J., & Kozlovsky, B.-Z. 1969, ApJ, 155, 1077
Blandford, R. D., & McKee, C. F. 1982, ApJ, 255, 419
Bracewell, R. N. 1986, The Fourier Transform and its Applications (2d ed.; McGraw-Hill: New York)
Clavel, J., et al. 1991, ApJ, in press
Collin-Souffrin, S., & Lasota, J.-P. 1988, PASP, 100, 1041
Cutri, R., et al. 1985, ApJ, 296, 423
Czerny, B., & Elvis, M. 1987, ApJ, 321, 305
Davidson, K., & Netzer, H. 1979, Rev. Mod. Phys., 51, 715
Deeter, J. E., & Boynton, P. E. 1982, ApJ, 261, 337
Edelson, R. A., & Krolik, J. H. 1988, ApJ, 333, 646
Edelson, R. A., Krolik, J. H., & Pike, G. F. 1990, ApJ, 359, 86
Edelson, R. A., & Malkan, M. A. 1986, ApJ, 308, 59
Gass, J. E., & Thompson, R. W. 1985, NASA IUE Newsletter, No. 28, p. 102
Huchra, J. P. 1990, private communication
Kallman, T. R., & Krolik, J. H. 1986, ApJ, 308, 805
Kallman, T. R., & McCray, R. M. 1982, ApJS, 50, 263
Krolik, J. H., & Kallman, T. R. 1984, ApJ, 286, 366
———. T. R. 1988, ApJ, 324, 714
Krolik, J. H., McKee, C. F., & Tarter, C. B. 1981, ApJ, 249, 422
Kwan, J. Y., & Krolik, J. H. 1979, ApJ, 233, L91
———. 1981, ApJ, 250, 478

Lawrence, A., Watson, M. G., Pounds, K. A., & Elvis, M. G. 1987, Nature 325, 694
Madau, P. 1988, ApJ, 327, 116
Malkan, M. A. 1988, Adv. Space Res., 8, 49
Malkan, M. A., & Filippenko, A. 1983, ApJ, 275, 477
McAlary, C. W., & Rieke, G. 1988, ApJ, 333, 1
McHardy, I. M., & Czerny, B. 1987, Nature, 325, 696
Osterbrock, D. E., & Parker, R. A. R. 1984, ApJ, 143, 268
Peterson, B. 1991, ApJ, in press
Peterson, B. M., Korista, K. T., & Cota, S. A. 1987, ApJ, 312, L1
Peterson, B. M., Reichert, G. A., Korista, K. T., & Wagner, R. M. 1990, ApJ, 352, 68
Pringle, J. 1981, ARA&A, 19, 137
Reichert, G., et al. 1991, in preparation
Roberts, D. H., Lehár, J., & Dreher, J. W. 1987, AJ, 93, 968
Rosenblatt, E. I., & Malkan, M. A. 1990, ApJ, 350, 132
Scargle, J. 1982, ApJ, 263, 835
Shuder, J. M. 1982, ApJ, 259, 48
Skilling, J., & Bryan, R. K. 1984, ApJ, 211, 111
Stirpe, G. M., de Bruyn, A. G., & van Groningen, E. 1988, A&A, 200, 9
Sun, W.-H., & Malkan, M. A. 1989, ApJ, 346, 68
Turner, M., & Pounds, K. A. 1989, MNRAS, 240, 833
Wamsteker, W., et al. 1990, ApJ, 354, 446
Wandel, A., & Petrosian, V. 1988, ApJ, 329, L11
Weisheit, J. C., Shields, G. A., & Tarter, C. B. 1981, ApJ, 245, 406